# Pseudouridine selects RNAs for extracellular transport

Alessandro Scacchetti[1†], Tuan D. Tran[1], Emily J. Shields[1], Lauren N. Reich[1], John F. Doherty[1], Julia A. Tasca[1], Grace E. Lee[2,3], Alejandro A. Vilcaes[4], Richard Lauman[1], Natali L. Chanaday[4], Benjamin A. Garcia[5], Colin C. Conine[2,3], and Roberto Bonasio[1†]

[1]Epigenetics Institute and Department of Cell and Developmental Biology; University of Pennsylvania Perelman School of Medicine, Philadelphia, Pennsylvania, USA.

[2]Departments of Genetics and Pediatrics; Epigenetics Institute; Institute of Regenerative Medicine; Center for Research on Reproduction and Women's Health; University of Pennsylvania Perelman School of Medicine, Philadelphia, Pennsylvania, USA.

[3]Division of Neonatology; Children's Hospital of Philadelphia, Philadelphia, Pennsylvania, USA.

[4]Departments of Physiology and Neuroscience; University of Pennsylvania Perelman School of Medicine, Philadelphia, Pennsylvania, USA.

[5]Department of Biochemistry and Molecular Biophysics; Washington University School of Medicine, St. Louis, Missouri, United States

[†]To whom correspondence should be addressed: roberto@bonasiolab.org; metalsga@gmail.com

**SUMMARY**

RNAs move through the extracellular space to transmit information between cells, including mammalian neurons, yet how specific RNAs are channeled into these extracellular routes is unknown. Using genome-wide CRISPR screening, proteomics, and high-sensitivity transcriptomics in a neuronal model system, we identify domesticated retroviral proteins and RNA-modifying enzymes that regulate RNA loading into and transportation via extracellular vesicles. We show that the pseudouridine synthase PUS1 is a key determinant of RNA trafficking, and that its catalytic product in RNA, pseudouridine, is enriched in extracellular RNAs from transformed and primary neurons. Furthermore, the presence of pseudouridine on select RNAs is both necessary and sufficient for their extracellular export. Finally, we show that myosin light chain 6 (MYL6) is a pseudouridine-binding protein required for secretion of synthetic and endogenous RNAs. These findings reveal a biochemical code linking chemical RNA modification to extracellular transport, and establish a framework to study the function of extracellular RNAs in the nervous system and beyond.

## INTRODUCTION

Cells exchange information to coordinate their actions. In addition to hormones, neurotransmitters, and other small molecules, RNAs also cross the plasma membrane and traverse the extracellular space to exert regulatory functions across cellular, tissue, and sometimes organismal boundaries[1-6]. In mammals, such intercellular transfer of RNA has been associated with diverse physiological and pathological processes, including brain function and disease[7-10], cancer[11] and intergenerational epigenetic inheritance[12], but its mechanistic bases remain obscure. Here, we investigate how RNAs are selected for extracellular export, a necessary step toward understanding what type(s) of information they communicate between cells, and determining whether and how this process affect phenotypic, transcriptional, and epigenetic states.

Extracellular RNAs (exRNAs) are often found within extracellular vesicles (EVs), membrane-based particles of heterogenous size, origin, and composition[13,14], produced by most cell types[15], and capable of transferring their cargo between cells[16]. Other structures, including membrane-free ribonucleoprotein complexes[17,18] and virus-like particles[19-23], can also transport RNA through the extracellular environment, although these processes are even less well understood than those mediated by canonical EVs.

The exRNAs produced by a given cell type do not recapitulate its intracellular RNA content[24-28], suggesting the existence of molecular pathways that facilitate (select) or prevent (filter) the release of specific RNAs in the extracellular environment. Mechanisms for exRNA selection have been proposed, including sequence-specific sorting mediated by RNA-binding proteins[27,29-33] and selective processing of exRNAs after their release[34-36]. To date, mechanistic studies have focused on extracellular transport mechanisms for microRNAs (miRNAs), largely in non-neuronal cells. However, miRNAs are relatively scarce in EVs[37], and it is becoming increasingly clear that neurons might have specialized strategies to select and release exRNAs[19,20,23,38]. Hence, the full spectrum of mechanisms that participate in exRNAs selection and transport, especially in neurons, remain unknown.

Here, we report a novel genetic screen that uncovered new regulators of exRNA export in a neuronal cell line. These include domesticated retroviral proteins and RNA-modifying enzymes. Among the latter, we show that the pseudouridine synthetase 1 (PUS1) and its catalytic product, pseudouridine (Ψ), are necessary and sufficient for the selection and extracellular release of certain exRNAs, including full-length transfer RNAs (tRNAs) and small nucleolar RNAs

47 (snoRNAs), through a process that also requires the non-canonical pseudouridine binding protein
48 myosin light chain 6 (MYL6).

49 **Neuronal CADs produce RNA-containing EVs**

50 To investigate the genetic and biochemical determinants of neuronal exRNA biogenesis in a
51 tractable model, we selected Cath.a-differentiated cells (CADs), an immortalized cell line that
52 resembles catecholaminergic neurons and is capable of forming neurite-like structures under
53 serum-free conditions[39-41]. We isolated EVs from conditioned, serum-free medium from CAD
54 cultures using an established serial ultracentrifugation method (**Fig. 1A**)[42]. This relatively crude
55 EV fraction consisted primarily of particles ranging from 90 to 150 nm in diameter (median 123
56 nm, **Fig. 1B**), consistent with the expected size range of small EVs[13]. This fraction was enriched
57 for known EV markers (SDCBP, PDCD6IP/ALIX, TSG101, CD9), and depleted for conventional
58 control mitochondrial and ER proteins (COXB5 and CANX) (**Fig. 1C**)[43]. Overall, 81% of the
59 proteins enriched in our EV isolate also appeared in a curated database of EV components
60 (Vesiclepedia, **Fig. S1A**)[44], and gene ontology (GO) annotations for the proteins we identified in
61 CAD EVs were enriched for relevant terms, including "*intracellular vesicle*" and "*endosome*" (**Fig.**
62 **S1B**). Consistent with the neuronal identity of CADs, GO terms associated with neurons ("*synaptic*
63 *membrane*", "*axon*") were also enriched, as well as specific neuronal EV markers L1CAM and
64 ATP1A3[45] (**Fig. 1C**, **Table S1**).

65 In contrast to the intracellular RNA composition of CADs, their EVs contained predominantly small
66 RNA species (< 500 nts; **Fig. 1D**), as previously observed in other neuronal EVs[46]. Because
67 conventional, ligation-based protocols to sequence small RNAs were largely developed to detect
68 miRNAs[47,48], we used LIDAR sequencing[49], which captures a broader range of RNAs regardless
69 of their size and chemical modifications, to obtain a comprehensive profile of the exRNAs
70 produced by CADs. LIDAR revealed 2,854 RNAs that were significantly (adjusted $p < 0.1$)
71 enriched in EVs compared to whole-cell extract (**Fig. 1E**). Compared to the intracellular
72 transcriptome, CAD exRNAs were enriched for nuclear tRNAs, Y-RNAs, and some small nuclear
73 RNAs (snRNAs), and depleted for mitochondrial tRNAs and miRNAs (**Fig. 1F; S1C**). Some
74 classes of snoRNAs such as the H/ACA box family were enriched in CAD EVs, whereas others,
75 such as C/D box snoRNAs were more abundant inside the cells (**Fig. S1D**). Further inspection of
76 the reads mapping to tRNA genes revealed the presence in EVs of a mixture of full-length tRNAs
77 and various types of tRNA-derived fragments (tDRs) (**Fig. S1E–F**).

78 To confirm that the exRNAs produced by CAD cells resided in the lumen of EVs, we exposed the
79 crude EV isolate to a mixture of RNase A and T1. A substantial amount of exRNAs resisted RNase
80 treatment in absence but not in presence of a detergent (Triton X-100), indicating that these
81 exRNAs resided in the lumen of membrane-delimited EVs (**Fig. S1G**). LIDAR sequencing after
82 RNase treatment of the EV isolate confirmed that most of the exRNAs we detected were not
83 simply associated with EVs, but were loaded into EVs as cargo and thus protected from
84 degradation by the EV membrane (**Fig. 1G**).

85 To extend our observation to *bona fide* neurons, we isolated EVs from cultured rat primary cortical
86 neurons, using a size-exclusion chromatography protocol[50], which yielded particles of size
87 comparable to those obtained from CADs (**Fig. S1H**). LIDAR sequencing of the RNA content of
88 these EVs revealed an enrichment for specific classes of RNAs, remarkably similar to those found
89 in CAD EVs (**Fig. 1H–I**), suggesting the existence of conserved mechanisms of neuronal exRNA
90 selection.

91 Thus, neuron-like CAD cells produce EVs that contain known EV-associated and neuronal
92 proteins, and are enriched in specific classes of RNA (including tRNAs and their fragments),
93 similar to EVs produced by primary neurons.

94 **Single-guide RNAs are loaded into EVs**

95 The fact that CAD EVs are enriched for specific RNAs when compared to their intracellular content
96 suggests the presence of dedicated pathways ensuring that only certain transcripts are selected
97 to become exRNAs. Potential mechanisms for both active and passive regulation of RNA
98 secretion have been proposed[51], but very few examples, seemingly dedicated to the export of
99 specific miRNAs, have been characterized[27,30,31,52]. It is unclear whether these bespoke pathways
100 also affect other RNA classes, which constitute the majority of exRNAs (**Fig. S1C**).

101 In search for general regulators of exRNA biogenesis, we performed a genome-wide knockout
102 screen. In a typical CRISPR/Cas9 screen, a library of single-guide RNAs (sgRNAs) targeting
103 genes of interest (or all genes in the case of genome-wide screens) is transduced into cells that
104 are then selected for a phenotype, for example drug resistance. Enriched or depleted sgRNAs
105 provide information on genes that regulate that phenotype and are identified by sequencing the
106 encoding transgenes integrated into the genome of the selected cells, thus linking genotypes to
107 phenotypes. This approach cannot be used for phenotypes not physically connected to the cell of
108 origin, such as EV abundance and composition.

109 We made the serendipitous observation that sgRNAs expressed from a lentiviral vector could be
110 detected in the crude EV fraction from CADs (**Fig. S2A**), therefore coupling the sgRNA genotype
111 of the originating cell to phenotypes associated with the sgRNA-containing EVs (**Fig. 2A, S2B**).
112 We reasoned that knockout of genes required for EV production or for loading RNAs into EVs
113 would result in the disappearance of the corresponding sgRNAs from the EV fraction, allowing us
114 to perform a genome-wide screen to identify genes involved in these processes.

115 We envisioned that targeted genes and the corresponding sgRNAs would fall within 4 possible
116 categories (**Fig. 2B**)**:** 1) sgRNAs not affecting viability, EV production, or RNA export ("no effect")
117 would remain constant over time in both cells and EVs; 2) sgRNAs targeting genes promoting
118 survival or proliferation would be depleted over time in both intracellular and extracellular pools
119 ("essential"); 3) positive regulators of EV production or RNA export would become less abundant
120 in the EV-associated pool over time, while possibly accumulating within cells ("positive"); and 4)
121 *vice versa* for negative regulators ("negative").

122 **A genome-wide screen for EV regulators**

123 We transduced CADs with the genome-wide Brie library, comprising ~80,000 sgRNAs targeting
124 ~20,000 protein-coding genes (**Fig. 2A**)[53]. Two days after infection, we harvested a fraction of the
125 cells and EVs to quantify baseline sgRNA distribution. Eight days later (day 10 after transduction),
126 we harvested cells and EVs again, and prepared libraries to sequence the sgRNAs, using a
127 modified LIDAR protocol (**Fig. S2C**). We performed the screen twice, obtaining two independent
128 experimental replicates.

129 Deep sequencing detected > 95% of sgRNAs in all samples (**Fig. S2D**). As early as day 2 after
130 transduction, likely before most knockout effects would manifest, not all sgRNAs were equally
131 represented in EVs compared to cells (**Fig. S2E**), indicating that some sgRNAs are more
132 efficiently loaded into EVs than others. This suggests that these exogenous RNAs are likely
133 subjected to the same selection processes that act on endogenous RNAs, potentially influenced
134 by differences in sequence, structure, or both. Consistent with this, sgRNAs that were
135 preferentially exported as exRNAs were characterized by a higher frequency of uridines at the 5'
136 (**Fig. S2F**), raising the possibility that these uridines, or perhaps their chemical modification, might
137 contribute to the selection process.

138 We analyzed the relative changes in abundance of sgRNAs in cells and EVs over time and sorted
139 the sgRNAs in the four categories described above (**Fig. 2C**). As expected, most sgRNAs were
140 neither enriched nor depleted ("no effect"), while sgRNAs targeting reported essential genes, such

141 as *Pcna*, *Cdk1*, and *Rrm1* were depleted at day 10 compared to day 2, both in cells and in EVs
142 ("essential"). Single-guide RNAs targeting tetraspanins, *Cd63*, *Tspan6*, and *Tspan15* were
143 depleted at day 10 in EVs, but not inside the cells, where they were either unchanged or enriched.
144 These genes might function as positive regulators of EV biogenesis ("positive"), in line with their
145 known role in membrane trafficking[54]. Conversely, we observed an enrichment of sgRNAs in EVs,
146 but not in cells, ("negative") for two subunits of ESCRT complexes, *Tsg101* and *Hgs* (*Hrs*),
147 consistent with recent reports suggesting that they may function as negative regulators for release
148 of some EV subtypes[55,56]. *Vps51*, encoding a subunit of the GARP complex[57], was also classified
149 by our screen as a negative regulator, likely due to its role in mediating retrograde trafficking from
150 early endosomes to the Golgi apparatus[58].

151 For each sgRNA, we calculated a "predicted" abundance in EVs compared to cells at day 10
152 based on its export efficiency measured at day 2 and then determined deviations from this
153 predicted value in the "observed" sgRNA abundances. Overall, we identified 1,275 and 1,228
154 genes targeted by significantly ($p$ value < 0.05) depleted or enriched sgRNAs (**Fig. 2D; Table**
155 **S2**), and therefore likely to function as positive or negative regulators of exRNA
156 selection/transport, respectively. Overall, the candidate positive regulators in our screen were
157 enriched for GO terms related to known EV biogenesis routes, such as "*late endosome*",
158 "*multivesicular body*", and "*extracellular vesicle*" (**Fig. 2E**), and comprised various genes involved
159 in the regulation of EV production and release (*Tspan6*, *Cd63*, *Flot1*, *Smpd3*, *Vps37c*, *Chmp2a*,
160 *Chmp5*, and *Chmp7*) (**Fig. 2D**). Among these, *Sdcbp* (**Fig. 2D; S2G**) stood out because of its
161 demonstrated role in EV biogenesis[59], established use as marker for these structures[43], and
162 abundance in CAD EVs (**Fig. 1C**). To confirm its function in neuronal EVs, we generated two
163 independent *Sdcbp*$^{-/-}$ CAD clones (**Fig. S2H**). Loss of SDCBP caused reduced particle numbers
164 indicative of impaired EV production, consistent with the effects observed in other cell types[59]
165 (**Fig. S2I–J**).

166 Given that our screen utilized extracellular sgRNAs directly as a readout, the identification of
167 *Sdcbp* suggests that sgRNAs are exported, at least in part, via EVs originating from a variation of
168 the ESCRT pathway[59]. However, several genes encoding domesticated retroviral proteins (*Arc,*
169 *Moap1, Nynrin, Pnma8b, Rtl5, Rtl8b*)[60] were also among the top candidates for positive regulators
170 of sgRNA export (**Fig. 2F**). Encapsulation of RNAs in capsid-like structures could therefore
171 represent an alternative route for exRNA export, potentially one reserved for neuronal cells[19,20,61-
172 63], given that several of these genes are preferentially expressed in the nervous system[60].
173 Consistent with neuronal-biased expression, all these candidates except *Moap1* (for which our

174 RNA-seq was not sufficiently sensitive) were upregulated upon differentiation of CADs into a more
175 mature neuronal phenotype (**Fig. S2K**)[39,40].

176 Our screen also identified positive regulators with no obvious link to membrane trafficking. We
177 reasoned that some of these factors might be involved in RNA selection or loading into the EVs
178 and that, therefore, their depletion would cause the disappearance of the corresponding sgRNAs
179 over time. Amongst them, we noted several enzymes responsible for installing or removing
180 chemical modifications on RNA, including pseudouridine (*Pus1, Rpusd2*)[64], wybutosine (*Tyw1*)[65],
181 acp(3)uridine (acp$^3$U) (*Dtwd1*) [66], mannosyl-queuosine (*Gtdc1*)[67], inosine (*Adarb1*)[68] , methyl
182 groups (*Mrm2*) [69], and amino acids (*Vars1, Tars1, Tars2, Dtd2, Prorsd1*)[70-72] (**Fig. 2G**). More
183 broadly, we identified 224 RNA-binding proteins amongst the positive exRNA regulators via
184 RBP2GO analysis[73] (**Table S3**), in line with our expectations that factors involved in the selection
185 and loading of RNAs into EVs would be revealed by our genetic screen.

186 In summary, we devised a pooled genome-wide strategy to link genetic perturbation to regulation
187 of exRNA export. We identified several factors that could be promoting or restricting exRNA
188 selection and transport, including several domesticated retroviral genes, suggesting an
189 alternative, potentially neuron-specific mode of RNA secretion. Our screen also uncovered a
190 variety of RNA modifiers and RNA-binding proteins that could be involved in marking and
191 selecting specific RNAs for extracellular trafficking, as demonstrated below for PUS1.

192 **PUS1 shapes the exRNA population**

193 Among the RNA-modifying enzymes identified as candidate positive regulators of exRNAs, we
194 chose to focus on the pseudouridine (Ψ) synthase PUS1[64], as it was among the top 100 most
195 significant positive regulators (**Fig. 2D, G; Table S2**) and because genetic evidence has
196 implicated Ψ in RNA mobility in *Arabidopsis thaliana* pollen[74].

197 To validate the results of the screen, we utilized an orthogonal, pooled CRISPR interference
198 approach (CRISPRi)[75], whereby we knocked down genes of interest by repressing their
199 transcription with dCas9-KRAB guided by sgRNAs different from those used for the primary
200 screen (**Fig. S3A**). CRISPRi of *Pus1* in CADs suppressed the secretion of sgRNAs significantly
201 ($p$ = 0.01) and to a larger extent than the positive control *Sdcbp* (**Fig. S3B**), confirming its
202 involvement in exRNA export.

203 To determine the contribution of PUS1 to the export of endogenous RNAs, we profiled intra- and
204 extra-cellular RNAs in wild type CADs and two independent *Pus1*$^{-/-}$ clones (**Fig. 3A**). Loss of
205 PUS1 resulted in a significantly (adjusted $p < 0.1$) altered profile of 560 exRNAs, skewed more

206 than 2-fold toward reduced export (390 reduced vs. 170 increased exRNAs; **Fig. 3B**). Changes
207 in exRNA abundance were not secondary to altered levels of the corresponding transcripts inside
208 the cells, as shown by a negligible overlap in the affected RNA subsets (**Fig. 3C; S3C–E**). The
209 export of miRNAs, snoRNAs, and both mitochondrial and nuclear tRNAs was significantly
210 impaired in the absence of PUS1 compared to wild type (**Fig. 3D**). Further inspection of tRNA-
211 mapping reads revealed that full-length and 5' and 3' tRNA-derived fragments (tDRs; **Fig. 3E**)
212 were exported less efficiently into EVs in absence of PUS1, with the full-length transcripts being
213 most strongly affected (**Fig. 3F**).

214 We conclude that PUS1 is necessary for the secretion of certain RNAs, including miRNAs,
215 snoRNAs, and tRNAs, in CADs.

216 **Pseudouridine stimulates RNA secretion**

217 Based on our observation that PUS1 is required for the release of a subset of exRNAs, we
218 hypothesized that its catalytic product, Ψ, might guide certain RNAs to be incorporated into EVs,
219 facilitating their export into the extracellular space.

220 To determine if exRNAs contain Ψ , we incorporated the Ψ-bisulfite adduct production step from
221 BID-seq[76] into our high-sensitivity LIDAR approach[49]. This allowed us to identify Ψ through the
222 appearance of microdeletions in the sequencing reads (**Fig. 4A**), as demonstrated on a synthetic
223 RNA (**Fig. S4A**) and within endogenous 18S rRNA, which contains several known Ψ residues
224 (**Fig. S4B**)[76]. With this approach, we detected 1,111 Ψ sites on 466 distinct exRNAs from CADs
225 (**Fig. S4C–D**). As expected, most Ψ sites were within tRNAs both inside and outside the cells, but
226 RNAs from other classes also contained this modification (**Fig. 4B**), consistent with existing
227 observations[77]. The majority of exRNAs with detectable Ψ also carried this modification inside the
228 cells (**Fig. S4C**), in most cases at the same exact sites (**Fig. S4D**); however, we observed higher
229 Ψ levels on exRNAs compared to cellular RNAs (**Fig. 4C**), suggesting an association of the mark
230 with their extracellular export. We observed a significant ($p < 10^{-15}$) enrichment for
231 pseudouridylated RNAs also in EVs isolated from rat primary neuronal cultures via size-exclusion
232 chromatography (**Fig. 4D**), indicating that the role for Ψ in shaping the exRNA population is
233 conserved across neurons from different species and not a peculiarity of transformed CAD cells.

234 Next, we sought to determine whether Ψ was also enriched on exRNAs *in vivo* outside the
235 nervous system. One of the most consequential and intensely studied pathways of extracellular
236 RNA exchange in mammals occurs in the male reproductive tract, where RNAs are transferred to
237 the developing sperm via specialized EVs (epididymosomes) in a process necessary for proper

238 sperm function[78] and implicated in intergenerational inheritance[12]. We isolated RNAs from EVs
239 purified from the cauda section of the mouse epididymis, (**Fig. 4E; S4E**) and identified 1,976 Ψ
240 sites on mapping to 846 exRNAs. As observed in CADs and primary rat neurons, cauda exRNAs
241 also contained higher levels of Ψ compared to their intracellular counterparts (**Fig. 4E**),
242 demonstrating that Ψ is enriched on exRNAs not only *in vitro* in neurons (see **Fig 4C–D**), but also
243 in other tissues *in vivo*.

244 Given the enrichment of Ψ on exRNAs, we wondered if Ψ is sufficient to induce RNA secretion.
245 We *in vitro* transcribed 102 bp-long RNAs replacing all U's with Ψ. We transfected these Ψ-
246 containing RNA into CADs and measured their appearance in the extracellular space by RT-
247 qPCR after 24 hours (**Fig. 4F**). RNA containing Ψ was exported ~4 times more efficiently
248 compared to the U-containing control, despite their levels being the same inside the cells (**Fig.
249 4G**). We tested additional RNAs, differing in sequence at their 5' (**Table S5**) and for most of them
250 (4 out of 6 sequences tested) the presence of Ψ resulted in significantly increased abundance
251 outside the cells, with a fifth one (RNA #6) also showing a clear trend toward increased export
252 (**Fig. 4H**).

253 Our results strongly suggest that Ψ functions to stimulate export of at least certain subsets of
254 exRNAs in various cell types, both *in vitro* and *in vivo.*

255 **PUS1 regulates exRNA export via site-specific pseudouridylation**

256 Our genetic evidence linking PUS1 to exRNAs (**Fig. 2–3**) and sequencing and gain-of-function
257 experiments on Ψ (**Fig. 4**) support the hypothesis that conversion of U to Ψ by PUS1 facilitates
258 the secretion of select RNAs. To test this hypothesis, we sought to determine whether the loss of
259 PUS1-dependent Ψ in CADs would cause decreased export of specific exRNAs. Because Ψ can
260 also be deposited by other enzymes, we first identified uridines specifically modified by PUS1, by
261 comparing bisulfite-induced deletions in exRNAs from *Pus1*$^{-/-}$ vs. wild type CADs. We found 479
262 PUS1-sensitive Ψ sites on 270 transcripts, accounting for 43% of the total Ψ sites on exRNAs
263 (**Fig. 5A**). Decreased Ψ levels on these PUS1 targets did not affect their abundance inside the
264 cells compared to RNAs containing Ψ residues unaffected by PUS1 loss (**Fig. 5B**, left). However,
265 the abundance of PUS1 targets in the EVs from *Pus1*$^{-/-}$ CADs was significantly decreased (**Fig.
266 5B**, right) ($p$ = 0.008) suggesting that PUS1-mediated deposition of Ψ was required for their
267 efficient export.

268 The majority of exRNAs carrying PUS1-dependent Ψ were full-length tRNAs (**Fig. S5A–B**), which
269 were targeted by PUS1 specifically at position 27 and 28 of the anticodon stem (**Fig. S5C–E**), as

270 previously reported in other cell types[77]. Of the 8 full-length tRNAs that were significantly depleted
271 in EVs from *Pus1*$^{-/-}$ CADs, all but one (Fisher's test $p = 0.006$) contained a PUS1-dependent Ψ at
272 position 27 or 28 (**Fig. S5F**), as exemplified for *tRNA-Arg-CCG-3-1*, *tRNA-Arg-CCT-4-1, tRNA-*
273 *Ile-AAT-1-1,* and *tRNA-Val-CAC-2-1* (**Fig. 5C–D**)

274 Not all Ψ sites on these extracellular tRNAs were PUS1 sensitive, as shown by the persistence
275 of Ψ signal at other positions in *Pus1*$^{-/-}$ KOs (**Fig. S5D**), most notably base 54, which is modified
276 by PUS10 (**Fig. S5D–E**)[77]. This indicates that the role of Ψ in the export of these exRNAs is
277 context-dependent, and that sequence or structural features of the surrounding RNA (or possibly
278 additional RNA modifications) contribute to its function.

279 We observed a similar exRNA export defect in *Pus1*$^{-/-}$-derived EVs for snoRNAs (**Fig. S5G**),
280 although in this case only 6 out of 13 snoRNAs containing PUS1-sensitive sites displayed an
281 export defect in the knockout cells, as exemplified by *Snord59a* and *Snord87* (**Fig. 5E–F)**.

282 Together, these observations support the conclusion that Ψ deposition by PUS1 on specific RNAs
283 is necessary for their efficient extracellular export

284 **MYL6 mediates the secretion of Ψ-containing RNAs**

285 We hypothesized that one or more RNA-binding protein recognize Ψ-marked RNAs to channel
286 them into secretory pathways. We incubated biotinylated RNA containing Ψ's or only U's as
287 control with CAD whole-cell extracts, purified the RNA with streptavidin, and analyzed associated
288 proteins via mass spectrometry. 46 proteins bound specifically to Ψ-containing RNA compared to
289 the U-only control (**Fig. S6A; Table S4**)**,** among which the myosin light chain 6 (MYL6) was the
290 most enriched Ψ-specific binder (**Fig. 6A; Table S4**). MYL6 is an essential light chain component
291 of the non-muscle myosin II complex[79], and it was previously reported as a putative non-canonical
292 RNA-binding protein[80].

293 Consistent with a role in exRNA trafficking, MYL6 was enriched in the proteome from CAD EVs
294 (**Fig. 1C; Fig. S6B**) and sgRNAs against it were depleted in our screen, although slightly below
295 our significance threshold ($p = 0.053$) (**Fig. S6C**). We knocked down MYL6 in CADs (**Fig. S6D**)
296 and found that Ψ-dependent secretion of 2 out of 4 RNAs was substantially impaired, with a third
297 one also demonstrating a clear trend toward reduction (**Fig. 6B**). To determine whether MYL6
298 was also involved in the Ψ-dependent export of endogenous exRNAs, we performed LIDAR on
299 intra- and extra-cellular RNAs after MYL6 knockdown. The abundance of intracellular RNAs was
300 largely unaffected (**Fig. S6E**), regardless of their Ψ content (**Fig. 6C**, "cells"); however, the export
301 of Ψ-containing exRNAs in EVs was significantly impaired by MYL6 knockdown (**Fig. 6C–D, Fig.**

302 **S6F**). This decrease in Ψ-containing exRNAs upon MYL6 knockdown was also observed, and in
303 fact was more pronounced, after RNase treatment of the EV isolate (**Fig. 6C–D**), indicating that
304 the exRNAs affected by MYL6 depletion reside within the EV lumen.

305 Our results demonstrate that the presence of Ψ—a modification enriched on exRNAs *in vitro* and
306 *in vivo*—is sufficient to stimulate exRNA export, and that, in many cases, Ψ-dependent exRNA
307 sorting in EVs is an active process mediated by the non-canonical RNA-binding protein MYL6.

## 308 DISCUSSION

309 In this study, we combined biochemical, genetic, and genomic approaches to reveal a role for
310 PUS1 and MYL6 in guiding the extracellular traffic of RNAs via Ψ modification. We propose a
311 model whereby PUS1 converts U to Ψ at defined sites on select RNAs, which are then bound
312 by MYL6 to be packaged into EVs and secreted (**Fig. 6E**). In addition to PUS1 and MYL6, our
313 work points to many new candidate regulators that might play important roles in selecting (RNA-
314 modifying enzymes) and transporting (domesticated retroviral proteins) RNAs from neurons and
315 other cell types into the extracellular space.

### 316 A genome-wide screen for EV and exRNA regulators

317 We developed a CRISPR/Cas9 pooled genetic screen strategy that linked extracellular
318 phenotypes to cellular genotypes via direct sequencing of secreted sgRNAs (**Fig. 2; S2**). With
319 this design, we could identify not only factors that regulate EV biogenesis in general, but also
320 factors required for the selection, loading, and transport of exRNAs into EVs, and potentially other
321 non-canonical RNA-containing extracellular particles.

322 Two other screens aimed at separately addressing one or the other process have been published
323 to date. In one case, artificial tethering of sgRNAs though an EV-specific anchor (CD63-dCas9 or
324 CD9-dCas9) was used to create a readout for EV production[56], which limited the screen to the
325 discovery of factors regulating the biogenesis of these specific EV sub-populations containing
326 CD63 or CD9, and, by design, bypassed the factors required to load RNA into the EVs. In the
327 other, barcoded miRNAs containing the EXO motif[31] were used as reporters for miRNA secretion,
328 revealing the role of ARHGEF18 in regulating the release of miRNA-containing EVs[81]. In this latter
329 case, only factors involved in movement of this specific subset of exRNAs could be recovered.

330 While these two studies provided important insights into EV biogenesis and miRNA transport,
331 respectively, our unbiased screen cast a broader net for general regulator of all extracellular

332 particles containing exRNAs, as revealed by the extensive number of "hits" already known to take
333 part in membrane trafficking (**Fig. 2D–E**), and by the large number of candidates involved in RNA
334 biology, such as RNA-modifying enzymes (**Fig. 2G**), that have not been previously linked to RNA
335 secretion.

336 Importantly, ours was the first genetic screen for an EV phenotype to be conducted on a cell line
337 with neuronal identity, which, in addition to its unique and broader design, likely contributed to our
338 ability to detect several candidates not previously associated with exRNA trafficking and that
339 might be restricted—in expression or function—to the nervous system.

340 **Routes of exRNA secretion in neurons**

341 While we designed our genetic screen with the goal of uncovering specific regulators of exRNA
342 selection and export, the strategy allowed us to simultaneously identify several factors involved
343 in the biogenesis and trafficking of EVs as "by-products". The observation that SDCBP was
344 identified as positive regulator (**Fig. S2G–J**) suggests that sgRNAs (and likely other RNAs) taking
345 the extracellular route may be loaded into EVs formed through a variation of the canonical ESCRT
346 pathway, in which SDCBP acts in concert with ALIX to regulate the production of endosomal
347 intraluminal vesicles[59]. This is further supported by the presence of several components of the
348 ESCRTIII complex (CHMP2A, CHMP5, CHMP7) amongst the list of candidate positive regulators
349 (**Fig. 2D**). We also recovered factors potentially involved in alternative modes of exRNA secretion
350 in neuronal cells, such as intraluminal vesicles produced by endosomal membrane curvatures
351 induced by ceramide in lipid rafts[82], since both SMPD3 (nSmase2, responsible for ceramide
352 synthesis) and FLOT1 (enriched in lipid rafts) appeared amongst our positive regulators of
353 exRNAs (**Table S2**).

354 In line with the neuronal identity of CADs, but somewhat unexpectedly, we detected synaptic
355 components in our EV preparation (**Fig. 1D; Table S1**) and some of them (e.g.: CXADR, GNAO1,
356 CNR1, ADAM10) were also identified as exRNA regulators in our screen (**Fig. 2E; Table S2**).
357 This suggests that in mammalian neurons, some EVs are produced at the presynaptic membrane,
358 as observed in *Drosophila*[83,84], indicating the existence of dedicated alternative routes for
359 neuronal exRNAs. Interestingly, fly and mammalian neurons have been shown to package RNAs
360 for secretion in structures resembling viral capsids originating from domesticated retroviral
361 proteins[19,23,85], whose intercellular exchange appears important for synaptic function, as well as
362 learning and memory[86].

363 Among potentially neuron-specific regulators of exRNA trafficking, domesticated retroviral
364 proteins stand out as particularly intriguing, with six recovered in our screen (**Fig. 2F**). One of
365 these, ARC, is a GAG homolog that assembles into a virus-like particle that transports its own
366 mRNA across the plasma membrane in humans and flies[19,20,62]. Several additional genes with
367 homology to the retroviral GAG capsid protein or other retroviral components are under purifying
368 selection in mammalian genomes[60] and their expression is often high in differentiated neurons[87]
369 (and also see **Fig. S2K**), hinting at the tantalizing possibilities that brains have hijacked viral
370 machinery for the purpose of RNA-based communication.

371 **A role for Ψ on exRNAs**

372 Ψ is the most abundant RNA modification found in cells, and it is known for its roles in RNA
373 stability, translation, and splicing[88]. However, the very strong depletion of sgRNAs against PUS1
374 in our screen, as well as some indirect evidence in other organisms motivated us to explore a
375 potential role in exRNAs. In *Arabidopsis*, Ψ appears to participate to the transfer of small RNAs
376 from pollen to sperm cells[74]. In human colorectal cancer cells, decreased Ψ levels caused by 5-
377 fluorouracil treatment were linked to alteration of extracellular small RNA profiles[89]. In line with
378 these reports, we found Ψ to be: 1) enriched in exRNAs from CAD cells, rat neurons, and mouse
379 epididymis, 2) sufficient for export of most synthetic RNAs tested, and 3) required for the release
380 of endogenous RNA, especially tRNAs and snoRNAs, into the extracellular space.

381 How does Ψ promote RNA secretion? We propose that the conversion of U to Ψ creates new
382 binding sites for specific proteins that function as Ψ readers. We identified MYL6, part of the non-
383 muscle myosin II complex, as a new Ψ reader and demonstrated its functional involvement in
384 RNA export of synthetic and endogenous exRNAs marked by Ψ **(Fig. 6**). Intriguingly, another
385 cytoskeletal proteins, the actin-binding protein PFN1, has been reported to interact with Ψ in
386 vitro[90]. RNAs containing Ψ might thus "hitchhike" cytoskeletal components to be loaded into
387 vesicles and eventually secreted, a pathway already proposed for other vesicular cargo such as
388 actin-associated proteins[91]. It is worth noting, however, that not all Ψ-containing synthetic and
389 endogenous exRNAs were sensitive to MYL6 depletion. While this could be attributed to
390 experimental limitations (such as incomplete MYL6 knockdown), it is also possible that other Ψ
391 readers are involved, perhaps in an RNA sequence- or structure-dependent fashion.

392 PUS1 is a conserved eukaryotic standalone pseudouridine synthetase which has been
393 extensively characterized in *S. cerevisiae*[64], where it plays important roles in tRNA biogenesis[92].
394 In mammals, PUS1 localizes both to the nuclei and mitochondria[93]. Our work suggests that PUS1-

395 mediated Ψ has a previously unappreciated function: guiding the export of exRNAs. Knockout of
396 PUS1 in neuronal CADs resulted in a significant loss of Ψ from many RNAs and, importantly, in
397 non-overlapping effects on cellular and extracellular RNA pools (**Fig. 3**). PUS1 loss significantly
398 decreased secretion of full-length tRNAs, likely due to the loss of PUS1-dependent Ψ at position
399 27 and 28 in the anticodon stem. Interestingly, other Ψ sites remain intact, indicating that
400 modification at these other positions may not be sufficient for export (**Fig. 5; S5**) and that the
401 export-related function of Ψ depends on sequence or structural context.

402 **Chemical modifications for exRNA selection**

403 The most obvious class of candidate positive regulators of exRNAs revealed by our screen were
404 RNA-modifying enzymes (**Fig. 2**). Among these, we chose to focus on PUS1; however, not all
405 pseudouridylated exRNAs depend on PUS1 for their secretion, and many exRNAs do not contain
406 Ψ. We suspect that other RNA modifying enzymes contribute—independently or in concert with
407 PUS1—to shape the exRNA population in neurons and other cell types.

408 Among these other candidates, we note DTWD1, an enzyme responsible for $acp^3U$ deposition on
409 tRNAs and possibly other substrates[66]. $acp^3U$ is an attachment site for N-glycans[94], and
410 glycosylation of some RNAs seems to be important for their secretion through EVs[95], suggesting
411 that glycans could serve as alternative exRNA selection marks. Furthermore, we identified
412 ALKBH6 (**Table S2**), a poorly characterized protein predicted to have RNA demethylase activity[96],
413 as one of the top negative regulators (i.e.: factors that restrict exRNA export). A related RNA
414 demethylates ALKBH5 was recently shown to prevent RNA secretion via m6A removal[97], and we
415 speculate ALKBH6 may function similarly as a "filter" for exRNA export via modulation of RNA
416 methylation on yet unknown RNA substrates.

417 Our screen also uncovered hundreds of RNA-binding proteins that may regulate RNA secretion
418 without modifying them enzymatically (**Table S3**). Among these, we identified VAP-A, an
419 important regulator of exRNA export, previously reported to load RNAs into intraluminal vesicles
420 at contact sites between endoplasmic reticulum and multivesicular bodies[98]. We also identified
421 ANXA7, a protein involved in regulating membrane fusion during exocytosis[99] and recently
422 reported as an RNA binder[100]. Given its enrichment in CAD EVs (**Table S1**) and its reported
423 interaction with ESCRT-III[101], we postulate it may additional function as an RNA cargo loader
424 during EV formation. On the other hand, we failed to identify some other RNA-binding proteins
425 previously shown to modulate exRNA export, such as ALYREF, FUS, ATG7/12, SYNCRIP, YBX1,
426 and HNRNPA2B1[27,29-33]. This could be due to ineffectiveness of the corresponding sgRNAs, or

427 experimental differences in reporter RNA and cell type used. In fact, it seems possible that
428 different cell types would utilize different sets of RNA-binding proteins and RNA modifications to
429 guide the secretion of different classes of RNAs.

430 **Conclusions and outlook**

431 In conclusion, our screen in neuronal CADs discovered a new pathway for RNA secretion,
432 whereby PUS1 catalyzes the formation of Ψ on select RNAs, marking them for export via EVs,
433 through recognition by MYL6. The genetic identification and biochemical validation of this and
434 other mechanisms governing exRNA selection and transport will enable deeper mechanistic
435 investigation of their downstream biological functions, and, ultimately, help decode the language
436 of RNA-mediated cell-to-cell communication.

437

438 **MATERIALS AND METHODS**

439 **Cell culture and conditioned medium collection**

440 CADs (kind gift from S. Berger)[40] were maintained in DMEM/F-12 medium (Gibco, Cat. No
441 11320033) supplemented with 10% ES-grade fetal bovine serum (Gibco, Cat. No 16141079), 1%
442 L-Glutamine (Sigma-Aldrich, Cat. No G7513), and 0.5% penicillin/streptomycin solution (Sigma-
443 Aldrich, Cat. No P0781). EV-depleted fetal bovine serum was generated by centrifugation at
444 100,000 *g* (28,500 rpm) on a SW-32Ti swinging bucket rotor (Beckman Coulter, Cat. No
445 G369650) for 4 h at 4°C, followed by filtration through a 0.22 µm pore size filter (Sigma-Aldrich,
446 Cat. No S2GPU10RE). For EV collection, cells were seeded at 3–15 million per 15-cm dish and
447 washed twice with 1X PBS. Cells were incubated in serum-free medium (same as maintenance
448 medium but without fetal bovine serum) for 48 h (proteomics) or for 24 h (all other analyses)
449 before collecting EVs. For collection of EVs for pooled CRISPR screen (see below), cells were
450 incubated in EV-depleted medium (same as maintenance medium but with EV-depleted fetal
451 bovine serum) for 24 h. To obtain differentiated CADs, cells were maintained in serum-free
452 medium for 5 days.

453 **Animals**

454 Male FVB/NJ (8–12 weeks old) were derived from breeders obtained from Jackson Laboratory
455 (Strain #:001800) and maintained in-house. All animal procedures were in strict accordance with
456 the guidelines of the Children's Hospital of Philadelphia and the University of Pennsylvania
457 Institutional Animal Care and Use Committee regulations (CHOP IACUC Protocol #23-001364,
458 UPenn PSOM IACUC Protocol #806911).

459 Postnatal day 0-1 Sprague-Dawley rats (Charles River, SAS SD Strain Code 400) of both sexes
460 were used for generating primary neuron cultures. Experiments were performed following
461 protocols approved by the University of Pennsylvania Institutional Animal Care and Use
462 Committee (Protocol #: 807365). Rodents were euthanized following the Humane Euthanasia of
463 Laboratory Animals Standard Operating Procedures of the University of Pennsylvania.

464 **Dissociated cortical cultures from rats**

465 Bilateral cortices were chopped and digested using 10 mg/mL trypsin and 0.5 mg/mL DNAse for
466 10 min at 37°C. Tissue was carefully dissociated using a P1000 pipette and cells were plated onto
467 Matrigel (Corning, Cat. No 354234) coated plastic bottom 6-well plates. Neurons were grown
468 following our previously validated astrocyte-free culture approach[50]. Neurons were maintained in

469 Neurobasal (Gibco, Cat. No 21103049) supplemented with 2% B-27 (serum free, Gibco, Cat. No
470 17504044), 1 mM sodium pyruvate, 2 mM glutamine and 2 μM cytosine arabinoside.

471 **Extracellular vesicles (EV) isolation and nanoparticle tracking analysis**

472 EV isolation in CADs was performed via differential centrifugation, as previously described[42] with
473 minor modifications. Briefly, conditioned medium was centrifuged at 300 *g* for 5 min at 4°C,
474 followed by centrifugation at 2,000 *g* for 10 min at 4°C and then 10,000 *g* for 30 min at 4°C. Then,
475 the cleared conditioned medium was passed through a 0.22 μm pore size filter (Millipore-Sigma,
476 Cat. No SCGP00525) and centrifuged at 100,000 *g* (28,500 rpm) on a SW-32Ti swinging bucket
477 rotor for 2 h at 4°C. EV pellet was resuspended in 1X PBS and centrifuged again at 100,000 *g*
478 (28,500 rpm) on a SW-32Ti swinging bucket rotor for 2 h at 4°C. The washed EV pellet was then
479 resuspended in 100 μL of 1 X PBS and either used immediately or stored at -80°C.

480 Collection of EVs from rat neurons was performed when cortical cultures reached maturity after
481 14 days *in vitro* (DIV). At DIV 14, 50% of culture media was replaced and 30% of fresh media was
482 added every 24 h. After 60 h, culture supernatant was collected and cleared by serial
483 centrifugations as previously described[50]. The resulting supernatant was used for EVs isolation
484 by size exclusion chromatography using qEV1/35mm columns from IZON (Cat. No IC1-35) and
485 following the procedure suggested by the manufacturer and validated in our previous
486 publication[50].

487 For nanoparticle tracking analysis (NTA), EVs were diluted in deionized water and analyzed using
488 the ZetaView PMX220 Twin (Patricle Metrix) with the following parameters: laser wavelength =
489 488 nm; filter wavelength = scatter; shutter = 100; sensitivity = 80. NTA was performed at the
490 extracellular vesicle core at the University of Pennsylvania.

491 **Epidydimal tissue and EV collection**

492 Mice were sacrificed by cervical dislocation, and epididymal tissue carefully dissected free of fat
493 and connective tissue. The cauda epididymis was separated and immersed in pre-warmed (37°C)
494 Biggers, Whitten, and Whittingham (BWW) medium[102]. Seminal fluid was gently expressed from
495 the tissue. The tissue was removed from the media and flash frozen in a microcentrifuge tube and
496 kept at -80°C until processing for RNA isolation. The released spermatozoa were incubated in
497 BWW medium at 37 °C for 10 min to allow motile sperm to disperse. The suspension was
498 transferred to a fresh microcentrifuge tube and incubated for an additional 10 min at 37 °C to
499 enrich for motile sperm by swim-up. The upper fraction of the suspension was carefully aspirated,

500 leaving ~50 µL of residual medium behind. Spermatozoa were pelleted by centrifugation (10,000
501 *g*, 5 min), and the supernatant was centrifuged twice at 10,000 g for 5 min to remove residual
502 tissue and sperm, each time collecting only the supernatant. A final spin at 10,000 *g* for 30 min at
503 4 °C was performed to further eliminate debris. The resulting supernatant, containing EVs, was
504 subjected to ultracentrifugation (Optima Max TL, Beckman Coulter) at 120,000 *g* for 2 h at 4 °C.
505 The pellet was washed in 1 mL cold PBS and ultracentrifuged again at 120,000 *g* for 2 h at 4 °C.
506 The final epididymosome pellet was resuspended in 30 µL cold PBS, flash frozen in liquid
507 nitrogen, and stored at -80 °C until RNA isolation.

508 **Cells and EV proteomics**

509 EVs and cells were resuspended in freshly prepared, ice-cold urea lysis buffer (50 mM Tris pH 8,
510 8M urea) and incubated for 1 h at 4°C. Lysates were then sonicated using Bioruptor (Diagenode)
511 with 5 cycles of 30s on / 30 s off and then cleared by centrifugation at 18,000 *g* for 10 min at 4°C.
512 Extract was quantified using the Micro BCA Protein Assay Kit (Thermo Scientific, Cat. No 23235)
513 and 50 µg were taken for further processing. Proteins were prepared using Protifi S-trap Micro
514 columns per manufacturer's instructions. Following S-trap elution, peptides were lyophilized,
515 resuspended in 0.1 % formic acid for further cleanup by desalting. Desalted peptides were
516 lyophilized and resuspended in 4% acetonitrile containing 0.1% formic acid for LC-MS analysis.
517 Mass spectra for peptides were obtained with a Dionex Ultimate3000 liquid chromatograph
518 (Thermo Fisher Scientific) coupled to a Thermo Fusion mass spectrometer (Thermo Fisher
519 Scientific). Peptides were loaded onto an in-house silica capillary column (75 µM inner diameter)
520 packed with C18 resin (ReproSil-Pur C18-AQ 2.4-µm resin; Dr. Maisch GmbH, Ammerbuch,
521 Germany). Peptides were eluted with a gradient of 2%–25% B (86 min) followed by a gradient of
522 25%–50% (32 min) and a hold at 98% B (15 min) (mobile phase A: 0.1% formic acid, mobile
523 phase B: 80% acetonitrile, 0.1% formic acid). Flow rate was 300 nL/min. Data were collected in
524 data-dependent acquisition mode. Full-scan MS settings were as follows: scan range, 300–1,100
525 (m/z; mass-to-charge ratio); resolution, 60,000; AGC, on; micro scan count, 1; Maximum IT, 54
526 ms. MS2 settings were as follows: resolution, 30,000; AGC, predicted; micro scan count, 1;
527 Maximum IT, 100 ms; fragmentation was enforced by higher-energy collisional dissociation with
528 normalized collision energy of 29; isolation width, 1.8 m/z. MS/MS spectra were processed using
529 MetaMorpheus version (https://github.com/smith-chem-wisc/MetaMorpheus) using a UniProt *Mus*
530 *musculus* reference proteome and common contaminants. The following search settings were
531 used: protease = trypsin; search for truncated proteins and proteolysis products = false; maximum
532 missed cleavages = 2; minimum peptide length = 7; maximum peptide length = 60; initiator

533 methionine behavior = variable; fixed modifications = carbamidomethyl on C, carbamidomethyl
534 on U; variable modifications = oxidation on M; max mods per peptide = 1; max modification
535 isoforms = 1,024; precursor mass tolerance = ±10.0000 PPM; product mass tolerance = ±0.0200
536 absolute; report PSM ambiguity = true. Results were filtered for score (> 5) and FDR (1 %).

537 **RNA extraction**

538 Cell pellets or purified EVs were resuspended in 1 mL of TriPure (Roche, Cat. No 11667165001)
539 and RNA was extracted following the recommended protocol. DNA was digested with Turbo
540 DNase-I (Invitrogen, Cat. No AM2238) at 37˚C for 30 min, RNA was re-purified using TriPure and
541 resuspended in modBTE (10mM Bis-Tris pH 6.7, 0.1 mM EDTA). For RNA extraction directly from
542 cleared conditioned medium, 0.3 M NaOAc (final) and 1 volume of phenol-chloroform-IAA
543 (Ambion, Cat. No AM9732) were added and RNA was purified using the recommended protocol.
544 DNA was digested and RNA was re-purified using TriPure as described above.

545 For EVs from cultured primary rat neurons, RNA was extracted from pooled peak fractions using
546 phenol-chloroform-IAA as described for cleared conditioned medium.

547 **RNase digestion**

548 For RNase protection assays, ~$10^9$-$10^{10}$ EVs were incubated with 2 µg of RNase A + 5U of RNase
549 T1 (Thermo Fisher, Cat. No EN0551) in 100ul of PBS for 30 min at 25°C. Where indicated, Triton
550 X-100 was added to a final concentration of 1% v/v. Reactions were stopped by adding 10 µl of
551 murine RNase inhibitor (New England Biolabs, Cat. No M0314S), followed by incubation on ice
552 for 5 min. Then, 1 mL of TriPure (Roche, Cat. No 11667165001) was added and samples were
553 stored at -80°C. RNA was extracted as described above.

554 **LIDAR, small RNA-seq, and mRNA-seq libraries**

555 LIDAR libraries from 100–250 ng of cellular RNA or 1–50 ng of EV RNA were prepared as
556 described[49] with some minor modification. LIDAR_RT_primer and LIDAR_TSO_mix were diluted
557 1:3 for samples where RNA input was < 10 ng. Reverse transcription conditions were changed to
558 the following: 8°C for 10 min, 16°C for 10 min, 25°C for 10 min, 42°C for 80 min, 10 cycles at 50˚C
559 for 2 min and 42˚C for 2 min, 85°C for 5 min. Lastly, the amount of indexing primers was increased
560 to 10 pmol. LIDAR libraries were analyzed on a 2% agarose gel and quantified using Qubit dsDNA
561 Quantification Assay kit (Invitrogen, Cat. No Q32854).

562 Small RNA libraries were prepared using the NEBnext small RNA library kit for Illumina (New
563 England Biolabs, Cat. No E7330S), following the standard protocol with the following parameters:

564 1) 1:2 dilution of 3'SR Adaptor, SR RT Primer, and 5'SR Adaptor, 2) 15 indexing PCR cycles, 3)
565 cleanup of final libraries with QIAgen MinElute PCR purification kit (QIAgen, Cat. No 28004),
566 followed by a second cleanup with 2X SPRI. Libraries were analyzed on 6% non-denaturing
567 polyacrylamide gels.

568 Conventional mRNA-seq libraries were prepared from 2 µg of total CAD RNA following the
569 protocol described in[49].

570 Libraries were sequenced on Illumina NextSeq1000 or NextSeq2000 instruments.

571 **Genome-wide pooled CRISPR-Cas9 screen**

572 The mouse Brie sgRNA library[103] in the lentiCRISPR v2 and lentiGuide-Puro backbones were
573 obtained from Addgene (Cat. No 73632 and 73632). The library were amplified in ElectroMAX
574 Stbl4 competent cells (Invitrogen, Cat. No 11635018). To generate lentiviruses, ~100 million
575 HEK293FT were transfected with 275 µg of amplified library together with 170 µg of psPAX2
576 packaging plasmid (Addgene, Cat. No 12260) and 96 µg of pMDG.2 envelope plasmid (Addgene,
577 Cat. No 12259) using Lipofectamine 3000 Transfection Reagent (Invitrogen, Cat. No L3000015).
578 18 h after transfection, the medium was changed to lentivirus_collection_medium [DMEM high
579 glucose (Gibco, Cat. No 11965126) supplemented with 10% ES-grade fetal bovine serum (Gibco,
580 Cat. No 16141079), 1% GlutaMAX (Gibco, Cat. No 35050061), 1% MEM non-essential amino
581 acid solution (Sigma-Aldrich, Cat. No M7145-100ML), 1% sodium pyruvate (Millipore-Sigma, Cat.
582 No S8636), and 1% bovine serum albumin (Sigma-Aldrich, Cat. No A1933). Conditioned medium
583 was collected 48 h later, filtered through a 0.45 µm filter (Millipore-Sigma, Cat. No S2HVU11RE),
584 and concentrated using Amicon Ultra centrifugal filters with 100 kDa MWCO (Millipore-Sigma,
585 Cat. No UFC910008). Concentrated lentiviruses were aliquoted and stored at -80°C. Multiplicity
586 of infection (MOI) in CADs was estimated as described[104]. Briefly, CADs were infected with
587 increasing amounts of lentivirus using 8 µg/mL polybrene (final concentration). 24 h after infection,
588 cells were divided equally into two new wells and one of them was treated with 1 µg/mL puromycin
589 (Invivogen, Cat. No ant-pr-1). 96 h later, cells were counted, and the MOI was determined as the
590 percentage of surviving cells. To test for sgRNA presence in EV preparations, CADs were infected
591 with the Brie lentiGuide-Puro (sgRNA only) libraries at an MOI of 0.43 and ~1X coverage, selected
592 with 1 µg/ml puromycin for 7 days, and stably transduced cells were frozen in liquid $N_2$. RT-qPCR
593 for sgRNA expression was performed using Power SYBR Green RNA-to-$C_T$ (Applied Biosystems,
594 Cat. No 4389986) with the sgRNA_1_qPCR primers (**Table S5**).

595 The genome-wide screen was performed in 2 biological replicates. 55 million CADs were
596 transduced on day 0 with the lentiviral library at an MOI of 0.21 using 8 µg/mL polybrene to result
597 in ~100-150X sgRNA coverage. 24 h after infection, cells were washed twice with PBS and EV-
598 depleted medium was added. 24 h later ("day 2" throughout the manuscript), EVs and half the
599 cells were collected as described above and resuspended in TriPure. The other half of the cells
600 was re-plated with maintenance media containing 1 µg/mL puromycin. Cells were selected with
601 puromycin for 7 days. Then, cells were washed twice with PBS and EV-depleted medium was
602 added. 24 h later ("day 10" throughout the manuscript), EVs and cells were collected once again
603 and resuspended in TriPure. RNA was extracted from all samples as described. For cell samples,
604 < 200 nts RNAs were enriched using Zymo RNA Clean & Concentrator – 25 (Zymo Research,
605 Cat. No. R1017) following the recommended protocol.

606 sgRNA-seq libraries were prepared using a modified LIDAR protocol starting from half of the total
607 amount of RNA obtained from cells and EVs. In the case of cells, multiple parallel libraries were
608 prepared to not exceed 1.5 µg of input RNA / library, which were then pooled before sequencing.
609 Briefly, RNAs was diluted to 2.8 µL and mixed with 0.4 µL of 10 µM LIDAR_sgRNA_RT_primer
610 (see **Table S5** for all oligonucleotide sequences). Samples were heated to 70˚C for 2 min, then
611 cooled to 4˚C (0.5˚C/s). Next, 4.8 µL of RT_mix [25 mM Tris-HCl pH 8.3, 20 mM NaCl, 2.5 mM
612 $MgCl_2$, 8 mM DTT, 5% PEG-8000, 0.5 mM dNTPs, 1 mM GTP, 0.32 µL of 50 µM LIDAR_TSO
613 mix[49] or SS3_TSO, 0.5 U/µL murine RNase inhibitor (New England Biolabs, Cat. No M0314S),
614 and 2U/µL Maxima H-minus RT (Thermo Scientific, Cat. No EP0752); concentrations refer to a
615 final volume of 8 µL] were added. Reverse transcription was performed as follows: 42°C for 90
616 min, 10 cycles at 50˚C for 2 min and 42˚C for 2 min, 85°C for 5 min. cDNA was pre-ampified by
617 adding 12 µL of KAPA_mix [1X KAPA HiFi HotStart buffer Ready Mix (Roche, Cat. No KK2601),
618 1 µM LIDAR_preamp_f, and 0.1 µM LIDAR_preamp_r[49]; concentrations refer to a final volume of
619 20 µL] and by following these PCR cycling conditions: denaturation (95˚C for 3 min), 5 x (98˚C
620 for 20 s, 70˚C for 30 s, 72˚C for 30 s), final extension (72˚C for 5 min). Pre-amplified libraries were
621 purified using 2.5X SPRI beads (Beckman Coulter, Cat. No B23319) and eluted in 37 µL of TE
622 buffer (10mM Tris-HCl pH 8, 1 mM EDTA). 0.5 µL of each 10 µM custom Nextera indexing primers
623 was added, followed by 12 µL of Q5_mix [1X Q5 buffer, 0.5 mM dNTPs, 0.02 U/µL Q5 High-
624 Fidelity DNA Polymerase (New England Biolabs, Cat. No M0491); concentrations refer to a final
625 volume of 50 µL]. Samples were incubated with the following PCR cycling conditions: denaturation
626 (98˚C for 30 s), 15 x (98˚C for 10 s, 65˚C for 20 s, 72˚C for 20 s). Final libraries were purified using
627 2X SPRI beads (Beckman Coulter, Cat. No B23319) and eluted in 45 µL of TE buffer (10 mM
628 Tris-HCl pH 8, 1 mM EDTA). Libraries were analyzed on a 2% agarose gel and quantified using

629 Qubit dsDNA Quantification Assay kit (Invitrogen, Cat. No Q32854). Libraries were sequenced on
630 Illumina NextSeq500, NextSeq1000, or NextSeq2000 instruments.

631 **CRISPRi**

632 CRISPRi sgRNAs targeting the promoter region of *Sdcbp*, *Pus1,* and control (see **Table S5** for
633 all oligonucleotide sequences) were cloned in Lenti-(BB)-EF1a-KRAB-dCas9-P2A-BlastR
634 (Addgene, Cat. No 118154) using Golden Gate. To generate lentiviruses, ~0.5 million HEK293FT
635 in 6-well plates were transfected with 1.5 µg of CRISPRi plasmid together with 1 µg of psPAX2
636 packaging plasmid (Addgene, Cat. No 12260) and 0.5 µg of pMDG.2 envelope plasmid (Addgene,
637 Cat. No 12259) using Lipofectamine 3000 Transfection Reagent (Invitrogen, Cat. No L3000015).
638 24 h after transfection, medium was changed to lentivirus_collection_medium. Conditioned
639 medium was collected 48 h later, and cell and debris were removed by centrifugation at 500 *g* for
640 5 min, followed by 1,250 *g* for 5 min. Cleared conditioned medium containing lentivirus was
641 concentrated to 50 µL using Amicon Ultra Centrifugal Filter with 100 kDa MWCO (Millipore-Sigma,
642 Cat. No UFC5100). To generate stable CRISPRi cells, 50 thousand CADs were transduced with
643 50 µL of lentiviruses using 8 µg/mL polybrene (final concentration). 48 h after infection, medium
644 was supplemented with with 20 µg/mL blasticidin (Invivogen, Cat. No ant-bl-1) and cells were
645 selected for 4 days. To generate the pool of different CRISPRi cells, approximately equal number
646 of cells from individual knockdowns were mixed and cells were expanded in the presence of 20
647 µg/mL blasticidin. Cells were washed twice with PBS and EV-depleted medium was added. 24 h
648 later, conditioned medium was collected and cleared at 300 *g* for 5 min at 4°C, followed by
649 centrifugation at 2,000 *g* for 10 min at 4°C, 10,000 *g* for 30 min at 4°C, and concentration using
650 Amicon Ultra Centrifugal Filter with 100 kDa MWCO (Millipore-Sigma, Cat. No UFC5100). RNA
651 was extracted from cells and concentrated conditioned medium as described above. sgRNA-seq
652 libraries were prepared as described for the genome-wide screen using LIDAR_TSO_mix during
653 the reverse transcription. Libraries were sequenced on Illumina NextSeq1000 or NextSeq2000
654 instruments.

655 **Generation of Sdcbp-/- and Pus1-/- cells**

656 Single-guide RNAs targeting *Sdcbp* and *Pus1* (see **Table S5** for all oligonucleotide sequences)
657 were cloned in PX459 (Addgene, Cat. No 62988) using Golden Gate. 0.5 million CADs were
658 transfected with 2.5 µg of the targeting plasmids (PX459 backbone) using Lipofectamine 3000
659 Transfection Reagent (Invitrogen, Cat. No L3000015). 24 h after transfection, medium was
660 supplemented with 2 µg/mL puromycin, and cells were selected for 48 h. Next, cells were seeded

661 in 15-cm dishes at 500–1,000 cells per dish and incubated for 6 days without puromycin. Individual
662 colonies (corresponding to single clonal populations) were picked and transferred to 96-well
663 plates. Clones were expanded and tested by western blot to assess knock-out efficiency. Whole
664 cell extracts were prepared by lysis of cell pellets in RIPA buffer (10 mM Tris-HCl pH 8, 140 mM
665 NaCl, 1 mM EDTA, 0.1% Na-deoxycholate, 1% Triton-X-100, 0.1% SDS, 1X cOmplete EDTA-
666 free Protease Inhibitor), followed by sonication using Bioruptor (Diagenode) (30 s ON/OFF, 5
667 cycles) and clarification by centrifugation at 18,000 *g* for 10 min at 4°C.The following antibody
668 dilutions were used for western blots: 1:1000 for αSDCBP (Abcam, Cat. No ab19903), 1:500 for
669 αPUS1 (Abcam, Cat. No ab203010), 1:1000 for αSUZ12 (Cell Signaling Technology, Cat. No
670 3737S), 1:1000 for αTUBB (Abcam, Cat. No ab6046).

671 **Export of synthetic sgRNAs**

672 sgRNAs containing uridine or pseudouridine (Ψ) were synthesized by *in vitro* transcription. Briefly,
673 individual sgRNAs were PCR amplified to add a sense T7 promoter sequence (**Table S5**). RNA
674 was transcribed from ~500 ng of template DNA using HiScribe T7 High Yield RNA Synthesis Kit
675 (New England Biolabs, Cat. No E2040L) following the recommended protocol for short RNAs.
676 UTP was substituted with pseudo-UTP (Jena Bioscience, Cat. No NU-1139L) to generate Ψ-
677 containing sgRNAs. DNA was digested with Turbo DNase-I (Invitrogen, Cat. No AM2238) and
678 RNA was purified using TriPure (Roche, Cat. No 11667165001) as described above.

679 For assessing export with qPCR, 0.2 million CADs were transfected with 1 µg of UTP- or Ψ-
680 containing EGFP_1_sgRNA using Lipofectamine RNAiMAX Transfection Reagent (Invitrogen,
681 Cat. No 13778075). 6 h after transfection, cells were washed with serum-free medium, and then
682 incubated for additional 20 h in serum-free medium. Conditioned medium was collected and
683 cleared at 300 *g* for 5 min at 4°C, followed by centrifugation at 2,000 *g* for 10 min at 4°C and then
684 10,000 *g* for 30 min at 4°C. RNA was extracted from cells and cleared conditioned medium as
685 described above. RT-qPCR was performed using Power SYBR Green RNA-to-$C_T$ (Applied
686 Biosystems, Cat. No 4389986) with the EGFP_1_qPCR primers (**Table S5**). For assessing export
687 by sequencing, the same procedure was followed with some minor modifications. First, two
688 different sgRNA pools were created mixing 3 UTP-containing and 3 Ψ-containing sgRNAs (**Table**
689 **S5**). Second, 500 ng of sgRNA pools were used to transfect 0.3 million CADs. RNA was extracted
690 from cells and cleared conditioned medium as described above. sgRNA-seq libraries were
691 prepared using the same strategy as in the genome-wide screen. Libraries were sequenced on
692 Illumina NextSeq1000 or NextSeq2000 instruments.

693 **Bisulfite-modified LIDAR**

694 Bisulfite conversion and desulphonation of RNA was performed following the BID-seq protocol[76].
695 Briefly, input RNA (200 ng for cellular RNA and 10 ng for exRNAs) was diluted in 8.5 µL of water,
696 45 µL of freshly prepared BS reagent (2.4 M $Na_2SO_3$ and 0.36 M $NaHSO_3$) were added, and
697 samples were incubated at 70°C for 3 h. Next, 75 µL of water, 270 µL of RNA Binding Buffer
698 (Zymo Research, Cat. No. R1013), and 400 µL of 100% EtOH were added, and samples were
699 transferred on a Zymo column (Zymo Research, Cat. No. R1013). After washing with 200 µL of
700 RNA wash buffer, samples were incubated in-column with 200 µL of RNA desulphonation buffer
701 (Zymo Research, Cat. No. R5001-3-40) for 1 h and 15 min at 25°C. Samples were washed with
702 twice with RNA wash buffer (400 µL and 700 µL), then eluted in 6 µL of RNase-free water.
703 Libraries were prepared starting from half of the eluate using the LIDAR protocol described above
704 with a few modifications: 1) initial RNA denaturation was conducted at 72°C for 3 min; 2) $MgCl_2$
705 was substituted with $MnCl_2$ in the RT_mix (keeping the same amounts); 3) reverse transcription
706 conditions were changed to 8°C for 10 min, 16°C for 10 min, 25°C for 10 min, 42°C for 80 min,
707 10 cycles at 50˚C for 2 min and 42˚C for 2 min, 85°C for 5 min. Libraries from untreated RNA
708 input samples were prepared in parallel.

709 **RNA affinity chromatography**

710 Biotinylated sgRNAs containing U or Ψ were generated by *in vitro* transcription. Individual
711 sgRNAs were PCR amplified to add a sense T7 promoter sequence (**Table S5**). RNA was
712 transcribed from ~600 ng of template DNA (1:1 mix of EGFP_1_sgRNA and SCR_1_sgRNA)
713 using HiScribe T7 High Yield RNA Synthesis Kit (New England Biolabs, Cat. No E2040L) following
714 the recommended protocol for short RNAs. In all reactions, ATP was substitute with a 10:1 mix of
715 ATP and N6-(6-Aminohexyl)-ATP-Biotin (Jena Bioscience, Cat. No NU-805-BIO). UTP was
716 substituted with pseudo-UTP (Jena Bioscience, Cat. No NU-1139L) to generate Ψ-containing
717 sgRNAs. DNA was digested with Turbo DNase-I (Invitrogen, Cat. No AM2238) and RNA was
718 purified using TriPure (Roche, Cat. No 11667165001) as described above.

719 To prepare protein extracts, approximately 50 million CADs were collected and washed with PBS.
720 Cell pellets were resuspended in 1 mL of ice-cold CHAPS lysis buffer [50 mM Tris-Cl pH = 7.5,
721 150 mM NaCl, 0.5% CHAPS, 0.5 mM DTT, 1 X cOmplete EDTA-free Protease Inhibitor Cocktail
722 (Roche, Cat. No 11873580001)] and cells were lysed via 2 cycles of freezing in dry ice/EtOH bath
723 followed by rapid thawing at 37°C. Extract was clarified by centrifugation at 18,000 *g* for 10 min

724 at 4°C. Protein amounts were quantified using Bio-Rad Protein Assay Dye Reagent Concentrate
725 (Bio-Rad, Cat. No 5000006).

726 50 µg of U- or Ψ-containing biotinylated sgRNAs were mixed with 1 mg of CAD protein extract in
727 CHAPS lysis buffer supplemented with 1.5 mM $MgCl_2$ and the samples were rotated for 1 h at
728 room temperature. As a control, RNA was omitted from 1 reaction ("beads only"). Next, 50 µL of
729 Dynabeads MyOne Streptavidin C1 beads (Invitrogen, Cat. No 65001), equilibrated in CHAPS
730 lysis buffer supplemented with 1.5 mM $MgCl_2$, were added and samples were rotated for 1 h at
731 4°C. Beads were washed 3 X with medium salt buffer (50 mM Tris-Cl pH = 7.5, 150 mM NaCl,
732 1.5 mM $MgCl_2$, 0.5 mM DTT, 1 X cOmplete EDTA-free Protease Inhibitor Cocktail) and 3 X with
733 high salt buffer (50 mM Tris-Cl pH = 7.5, 500 mM NaCl, 1.5 mM $MgCl_2$, 0.5 mM DTT, 1 X cOmplete
734 EDTA-free Protease Inhibitor Cocktail). Proteins were prepared using Protifi S-trap Micro columns
735 per manufacturer's instructions. Following S-trap elution, peptides were lyophilized, resuspended
736 in 0.1 % formic acid for further cleanup by desalting. Desalted peptides were lyophilized and
737 resuspended in 4% acetonitrile containing 0.1% formic acid for LC-MS analysis. Mass spectra for
738 peptides were obtained with a Dionex Ultimate3000 liquid chromatograph (Thermo Fisher
739 Scientific) coupled to a Q-Exactive HF mass spectrometer (Thermo Fisher Scientific). Peptides
740 were loaded onto an in-house silica capillary column (75 µM inner diameter) packed with C18
741 resin (ReproSil-Pur C18-AQ 2.4-µm resin; Dr. Maisch GmbH, Ammerbuch, Germany). Peptides
742 were eluted with a gradient of 2%–25% B (85 min) followed by a gradient of 25%–50% (30 min)
743 and a hold at 98% B (15 min) (mobile phase A: 0.1% formic acid, mobile phase B: 80%
744 acetonitrile, 0.1% formic acid). Flow rate was 300 nL/min. Data were collected in data-
745 independent acquisition (DIA) mode had the following settings: Full scan MS – Scan range, 385–
746 1015 m/z; AGC target, 1e6; Ion inject time, 60 ms; Resolution, 60,000; Isolation width, 630.
747 MS/MS scan – Resolution, 30,000; MS2 AGC target, 1e6, Ion inject time, 60 ms; Isolation width,
748 24; HCD energy, 30. The reference proteomes used for data processing were the Uniprot Mus
749 musculus reference proteome and a Cas9 FASTA (UniprotID: Q99ZW2). DDA spectra were
750 processed with ProteomeDiscoverer (version 2.4.1.15) and Sequest. False discovery rates (FDR)
751 were estimated using a decoy database search with strict and relaxed target FDRs set to 0.01
752 and 0.05, respectively. DIA spectra were processed with DIA-NN (version 1.9.2). Outputs were
753 filtered at 0.01 FDR, which were estimated based on in silico-generated spectral libraries
754 generated by DIA-NN.

755 ***Myl6* knock-down**

siRNAs against *Myl6* and TYE 563 Control DsiRNA were obtained from Integrated DNA Technologies (Cat. No mm.Ri.Myl6.13.2, mm.Ri.Myl6.13.4, and TriFECTa RNAi Kit ). CADs were transfected with siRNAs using Lipofectamine RNAiMAX using 30-50 pmol of siRNA per million cells. Knockdown efficiency was measured 72 h after transfection via RT-qPCR using Power SYBR Green RNA-to-$C_T$ (Applied Biosystems, Cat. No 4389986) with the Myl6_qPCR primers (**Table S5**).

**Proteomics data processing and analysis**

Protein with measurable intensities only in cell or only in EV samples were excluded from the plot in **Fig. 1C** and denoted as "Cell-exclusive" or "EV-exclusive" in **Table S1**. Raw intensities were normalized using the `median_normalization` function or `proDA` package[105]. Differential abundance analysis was performed in R using the `limma` package as previously described[106,107]. Adjusted *p* values (FDR) were calculated using the `p.adjust` function (method = 'fdr'*)*. Gene ontology analysis was performed using DAVID (Cellular component 5)[108,109], including "EV-exclusive" proteins.

**Processing, mapping, and read counting (LIDAR, BID-LIDAR, small RNA-seq, mRNA-seq)**

Adapter trimming, UMI extraction, mapping to the *M. musculus* or *R. norvegicus* genome , deduplication and read counting for LIDAR, BID-LIDAR, and small RNA-seq (NEB) was performed exactly as described in[49] with scripts available on GitHub (https://github.com/bonasio-lab). For mRNA-seq libraries, paired-end reads were mapped directly using STAR[110] with the following parameters: `--peOverlapNbasesMin 10 --readMapNumber -1 --clip3pNbases 0 --alignIntronMax 100000 --outSAMtype BAM Unsorted`. Counts per gene were calculated in R using summarizeOverlaps function from GenomicAlignments. RNAs with 0 counts in all wild type samples (cellular or exRNAs) were excluded. Raw counts were batch corrected using `Combat_seq`[111].

**Processing, mapping and, read counting (sgRNA libraries)**

Adapter trimming on single-end reads was performed using `Cutadapt` [112] with the following parameters: `-a gttttagagcta -m 6`. UMI extraction was performed using the `process_files_single.sh` script available on GitHub (https://github.com/bonasio-lab) with the following parameters: 8bp (libraries constructed using SS3_TSO) or LIDAR (libraries constructed using LIDAR_TSO_mix). Reads were further trimmed with `Cutadapt` with the following parameter: `-u 1`. Reads were mapped to the reference sgRNA Brie library or the sgRNA

787 sequences used in "Export of synthetic sgRNAs" using `bowtie2`[113] using standard parameters
788 but specifying `--no-rc`. Aligned reads were deduplicated using `umi_tools`[114] with the following
789 parameter: `--method unique`. Reads shorter than 15 bp were filtered out using `bedtools`[115].
790 Read counting was performed from bam files using MAGeCK[116] with the following parameters:
791 `count`. Raw counts were batch corrected using `Combat_seq`[111].

792 **CRISPR screen analysis**

793 Batch corrected raw counts were normalized using MAGeCK with the following parameter: `count
794 -norm-method total`. Differential sgRNA abundance between cell and EVs at day 2 was
795 calculated with DESeq2[117] with the following parameter: `fitType = "local"`.

796 To identify candidates, first sgRNAs targeting genes not expressed in CADs (RPKM <1) were
797 excluded. Then, to account for individual sgRNA export efficiency as well as changes in sgRNA
798 representation in cells at day 10 due to fitness effects, we calculated a "predicted" sgRNA
799 abundance in day 10 EVs as follows:

800 $$i_{EV(day10)predicted} = average\left(\frac{i_{EV(day2)observed}}{i_{Cells(day2)observed}}\right) \times i_{Cells(day10)observed}$$

801 Where $i$ is the sgRNA read frequency in the indicated samples. Differences in EV sgRNA
802 predicted and observed abundance at day 10 were calculated using MAGeCK with the following
803 parameter: `test -paired`. GO analysis was performed using DAVID (cellular component, GO
804 level #5)[108,109].

805 **Differential RNA abundance analysis (LIDAR)**

806 Differential abundance between wild type cellular and exRNAs, as well as comparisons between
807 wild type and *Pus1*$^{-/-}$ mutant CAD, was performed using DESeq2[117] with the following parameter:
808 `fitType = "local"`. RNAs with an adjusted *p* value < 0.1 were considered differentially
809 enriched/exported.

810 **Analysis of Ψ with BID-LIDAR**

811 Detection of genomic positions with Ψ was done by identifying positions with deletions induced
812 by BID sequencing compared to a non-bisulfite-induced input. First, reads were mapped using
813 the LIDAR analysis pipeline, as described ab An in-house script using `GenomicRanges`[118],
814 `BioStrings` (https://bioconductor.org/packages/release/bioc/html/Biostrings.html), and
815 `bedtools`[115] was used to detect deletions within reads, map putative Ψ sites to the genome

816 reference, and calculate the fraction of reads at each genomic position that contain a deletion.
817 Only positions with at least 5% of reads deleted were considered to harbor a deletion. Positions
818 where deletion occurred 2 X more frequently in BID than input samples were classified as Ψ sites.
819 Position with a BID deletion rate in wild type < 0.75X compared to *Pus1*$^{-/-}$ were classified as PUS1-
820 sensitive Ψ sites. These positions were then assigned to the transcripts that contained them to
821 generate a list of modified RNAs.

822 For tRNA analysis of BID-LIDAR, the position of canonical bases for each tRNA gene were
823 annotated using the strategy described in[49]. These positions were used to identify tRNA
824 containing a U at position 27, which served as candidates for containing a Ψ at this position, and
825 to visualize and quantify reads with deletions at each canonical base.

826 **DATA AVAILABILITY**

827 Sequencing data is deposited in GEO: GSE320520. Proteomics data is deposited at PRIDE:
828 PXD069544 and PXD069598.

829 **ACKNOWLEDGMENTS**

830 The authors thank Andy J. Minn for technical advice, and Kenneth Zaret and the Bonasio lab for
831 feedback on the experiments and manuscript. R.B. acknowledges support from the NIH
832 (R35GM153281; DP1NS148061). C.C.C. acknowledges support from the NIH (R35GM151087)
833 This project was supported in part by a Penn Epigenetics Institute Pilot grant to R.B. and A.S.

834 **AUTHOR CONTRIBUTIONS**

835 Conceptualization: A.S. and R.B.; methodology: A.S., E.J.S., R.B. ; formal analyses: A.S., E.J.S.,
836 R.B.; investigation: A.S., T.D.T, E.J.S., L.N.R, J.F.D, J.T., G.E.L., A.A.V., R.L., N.C. ; data
837 curation: A.S., E.J.S., R.B.; writing – original draft: A.S. and R.B.; writing – review & editing: all
838 authors; visualization: A.S., E.J.S., R.B.; supervision: R.B., C.C.C., N.L.C., B.A.G.; project
839 administration: A.S. and R.B.; funding acquisition: R.B.

840 **COMPETING INTERESTS**

841 The authors declare no competing interest.

842 **REFERENCES**


843 1. Molnar, A., Melnyk, C.W., Bassett, A., Hardcastle, T.J., Dunn, R., and Baulcombe, D.C.
844 (2010). Small silencing RNAs in plants are mobile and direct epigenetic modification in
845 recipient cells. Science *328*, 872-875. 10.1126/science.1187959.

846 2. Betti, F., Ladera-Carmona, M.J., Weits, D.A., Ferri, G., Iacopino, S., Novi, G., Svezia, B.,
847 Kunkowska, A.B., Santaniello, A., Piaggesi, A., et al. (2021). Exogenous miRNAs induce
848 post-transcriptional gene silencing in plants. Nat Plants *7*, 1379-1388. 10.1038/s41477-
849 021-01005-w.

850 3. Cai, Q., Qiao, L., Wang, M., He, B., Lin, F.M., Palmquist, J., Huang, S.D., and Jin, H.
851 (2018). Plants send small RNAs in extracellular vesicles to fungal pathogen to silence
852 virulence genes. Science *360*, 1126-1129. 10.1126/science.aar4142.

853 4. Kaletsky, R., Moore, R.S., Vrla, G.D., Parsons, L.R., Gitai, Z., and Murphy, C.T. (2020).
854 C. elegans interprets bacterial non-coding RNAs to learn pathogenic avoidance. Nature
855 *586*, 445-451. 10.1038/s41586-020-2699-5.

856 5. Maori, E., Garbian, Y., Kunik, V., Mozes-Koch, R., Malka, O., Kalev, H., Sabath, N., Sela,
857 I., and Shafir, S. (2019). A Transmissible RNA Pathway in Honey Bees. Cell Rep *27*, 1949-
858 1959 e1946. 10.1016/j.celrep.2019.04.073.

859 6. Tassetto, M., Kunitomi, M., and Andino, R. (2017). Circulating Immune Cells Mediate a
860 Systemic RNAi-Based Adaptive Antiviral Response in Drosophila. Cell *169*, 314-325 e313.
861 10.1016/j.cell.2017.03.033.

862 7. Huo, L., Du, X., Li, X., Liu, S., and Xu, Y. (2021). The Emerging Role of Neural Cell-
863 Derived Exosomes in Intercellular Communication in Health and Neurodegenerative
864 Diseases. Front Neurosci *15*, 738442. 10.3389/fnins.2021.738442.

865 8. Marangon, D., Castro, E.S.J.H., and Lecca, D. (2022). Neuronal and Glial Communication
866 via Non-Coding RNAs: Messages in Extracellular Vesicles. Int J Mol Sci *24*.
867 10.3390/ijms24010470.

868 9. Wang, Z.Y., Wen, Z.J., Xu, H.M., Zhang, Y., and Zhang, Y.F. (2022). Exosomal noncoding
869 RNAs in central nervous system diseases: biological functions and potential clinical
870 applications. Front Mol Neurosci *15*, 1004221. 10.3389/fnmol.2022.1004221.

871 10. Budnik, V., Ruiz-Canada, C., and Wendler, F. (2016). Extracellular vesicles round off
872 communication in the nervous system. Nat Rev Neurosci *17*, 160-172.
873 10.1038/nrn.2015.29.

874 11. Moller, A., and Lobb, R.J. (2020). The evolving translational potential of small extracellular
875 vesicles in cancer. Nat Rev Cancer *20*, 697-709. 10.1038/s41568-020-00299-w.

876 12. Conine, C.C., and Rando, O.J. (2022). Soma-to-germline RNA communication. Nat Rev
877 Genet *23*, 73-88. 10.1038/s41576-021-00412-1.

878 13. Welsh, J.A., Goberdhan, D.C.I., O'Driscoll, L., Buzas, E.I., Blenkiron, C., Bussolati, B.,
879 Cai, H., Di Vizio, D., Driedonks, T.A.P., Erdbrugger, U., et al. (2024). Minimal information
880 for studies of extracellular vesicles (MISEV2023): From basic to advanced approaches. J
881 Extracell Vesicles *13*, e12404. 10.1002/jev2.12404.

882 14. van Niel, G., D'Angelo, G., and Raposo, G. (2018). Shedding light on the cell biology of
883 extracellular vesicles. Nat Rev Mol Cell Biol *19*, 213-228. 10.1038/nrm.2017.125.

884 15. Deatherage, B.L., and Cookson, B.T. (2012). Membrane vesicle release in bacteria,
885 eukaryotes, and archaea: a conserved yet underappreciated aspect of microbial life. Infect
886 Immun *80*, 1948-1957. 10.1128/IAI.06014-11.

887 16. O'Brien, K., Breyne, K., Ughetto, S., Laurent, L.C., and Breakefield, X.O. (2020). RNA
888 delivery by extracellular vesicles in mammalian cells and its applications. Nat Rev Mol Cell
889 Biol *21*, 585-606. 10.1038/s41580-020-0251-y.

890 17. Murillo, O.D., Thistlethwaite, W., Rozowsky, J., Subramanian, S.L., Lucero, R., Shah, N.,
891 Jackson, A.R., Srinivasan, S., Chung, A., Laurent, C.D., et al. (2019). exRNA Atlas
892 Analysis Reveals Distinct Extracellular RNA Cargo Types and Their Carriers Present
893 across Human Biofluids. Cell *177*, 463-477 e415. 10.1016/j.cell.2019.02.018.

894 18. Tosar, J.P., and Cayota, A. (2020). Extracellular tRNAs and tRNA-derived fragments. RNA
895 Biol *17*, 1149-1167. 10.1080/15476286.2020.1729584.

896 19. Pastuzyn, E.D., Day, C.E., Kearns, R.B., Kyrke-Smith, M., Taibi, A.V., McCormick, J.,
897 Yoder, N., Belnap, D.M., Erlendsson, S., Morado, D.R., et al. (2018). The Neuronal Gene
898 Arc Encodes a Repurposed Retrotransposon Gag Protein that Mediates Intercellular RNA
899 Transfer. Cell *172*, 275-288 e218. 10.1016/j.cell.2017.12.024.

900 20. Ashley, J., Cordy, B., Lucia, D., Fradkin, L.G., Budnik, V., and Thomson, T. (2018).
901 Retrovirus-like Gag Protein Arc1 Binds RNA and Traffics across Synaptic Boutons. Cell
902 *172*, 262-274 e211. 10.1016/j.cell.2017.12.022.

903 21. Moore, R.S., Kaletsky, R., Lesnik, C., Cota, V., Blackman, E., Parsons, L.R., Gitai, Z., and
904 Murphy, C.T. (2021). The role of the Cer1 transposon in horizontal transfer of
905 transgenerational memory. Cell *184*, 4697-4712 e4618. 10.1016/j.cell.2021.07.022.

906 22. Segel, M., Lash, B., Song, J., Ladha, A., Liu, C.C., Jin, X., Mekhedov, S.L., Macrae, R.K.,
907 Koonin, E.V., and Zhang, F. (2021). Mammalian retrovirus-like protein PEG10 packages
908 its own mRNA and can be pseudotyped for mRNA delivery. Science *373*, 882-889.
909 10.1126/science.abg6155.

910 23. M'Angale, P.G., Lemieux, A., Liu, Y., Wang, S., Zinter, M., Alegre, G., Simkin, A., Budnik,
911 V., Kelch, B.A., and Thomson, T. (2025). Capsid transfer of the retrotransposon Copia
912 controls structural synaptic plasticity in Drosophila. PLoS Biol *23*, e3002983.
913 10.1371/journal.pbio.3002983.

914 24. Valadi, H., Ekstrom, K., Bossios, A., Sjostrand, M., Lee, J.J., and Lotvall, J.O. (2007).
915 Exosome-mediated transfer of mRNAs and microRNAs is a novel mechanism of genetic
916 exchange between cells. Nat Cell Biol *9*, 654-659. 10.1038/ncb1596.

917 25. Mittelbrunn, M., Gutierrez-Vazquez, C., Villarroya-Beltri, C., Gonzalez, S., Sanchez-Cabo,
918 F., Gonzalez, M.A., Bernad, A., and Sanchez-Madrid, F. (2011). Unidirectional transfer of
919 microRNA-loaded exosomes from T cells to antigen-presenting cells. Nat Commun *2*, 282.
920 10.1038/ncomms1285.

921 26. Cha, D.J., Franklin, J.L., Dou, Y., Liu, Q., Higginbotham, J.N., Demory Beckler, M.,
922 Weaver, A.M., Vickers, K., Prasad, N., Levy, S., et al. (2015). KRAS-dependent sorting of
923 miRNA to exosomes. Elife *4*, e07197. 10.7554/eLife.07197.

924 27. Shurtleff, M.J., Yao, J., Qin, Y., Nottingham, R.M., Temoche-Diaz, M.M., Schekman, R.,
925 and Lambowitz, A.M. (2017). Broad role for YBX1 in defining the small noncoding RNA
926 composition of exosomes. Proc Natl Acad Sci U S A *114*, E8987-E8995.
927 10.1073/pnas.1712108114.

928 28. Upton, H.E., Ferguson, L., Temoche-Diaz, M.M., Liu, X.M., Pimentel, S.C., Ingolia, N.T.,
929 Schekman, R., and Collins, K. (2021). Low-bias ncRNA libraries using ordered two-
930 template relay: Serial template jumping by a modified retroelement reverse transcriptase.
931 Proc Natl Acad Sci U S A *118*. 10.1073/pnas.2107900118.

932 29. Shurtleff, M.J., Temoche-Diaz, M.M., Karfilis, K.V., Ri, S., and Schekman, R. (2016). Y-
933 box protein 1 is required to sort microRNAs into exosomes in cells and in a cell-free
934 reaction. Elife *5*. 10.7554/eLife.19276.

935 30. Garcia-Martin, R., Wang, G., Brandao, B.B., Zanotto, T.M., Shah, S., Kumar Patel, S.,
936 Schilling, B., and Kahn, C.R. (2022). MicroRNA sequence codes for small extracellular
937 vesicle release and cellular retention. Nature *601*, 446-451. 10.1038/s41586-021-04234-
938 3.

939 31. Villarroya-Beltri, C., Gutierrez-Vazquez, C., Sanchez-Cabo, F., Perez-Hernandez, D.,
940 Vazquez, J., Martin-Cofreces, N., Martinez-Herrera, D.J., Pascual-Montano, A.,
941 Mittelbrunn, M., and Sanchez-Madrid, F. (2013). Sumoylated hnRNPA2B1 controls the
942 sorting of miRNAs into exosomes through binding to specific motifs. Nat Commun *4*, 2980.
943 10.1038/ncomms3980.

944 32. Leidal, A.M., Huang, H.H., Marsh, T., Solvik, T., Zhang, D., Ye, J., Kai, F., Goldsmith, J.,
945 Liu, J.Y., Huang, Y.H., et al. (2020). The LC3-conjugation machinery specifies the loading
946 of RNA-binding proteins into extracellular vesicles. Nat Cell Biol *22*, 187-199.
947 10.1038/s41556-019-0450-y.

948 33. Santangelo, L., Giurato, G., Cicchini, C., Montaldo, C., Mancone, C., Tarallo, R., Battistelli,
949 C., Alonzi, T., Weisz, A., and Tripodi, M. (2016). The RNA-Binding Protein SYNCRIP Is a
950 Component of the Hepatocyte Exosomal Machinery Controlling MicroRNA Sorting. Cell
951 Rep *17*, 799-808. 10.1016/j.celrep.2016.09.031.

952 34. Costa, B., Li Calzi, M., Castellano, M., Blanco, V., Cuevasanta, E., Litvan, I., Ivanov, P.,
953 Witwer, K., Cayota, A., and Tosar, J.P. (2023). Nicked tRNAs are stable reservoirs of tRNA

halves in cells and biofluids. Proc Natl Acad Sci U S A *120*, e2216330120. 10.1073/pnas.2216330120.

35. Tosar, J.P., Segovia, M., Castellano, M., Gambaro, F., Akiyama, Y., Fagundez, P., Olivera, A., Costa, B., Possi, T., Hill, M., et al. (2020). Fragmentation of extracellular ribosomes and tRNAs shapes the extracellular RNAome. Nucleic Acids Res *48*, 12874-12888. 10.1093/nar/gkaa674.

36. Nechooshtan, G., Yunusov, D., Chang, K., and Gingeras, T.R. (2020). Processing by RNase 1 forms tRNA halves and distinct Y RNA fragments in the extracellular environment. Nucleic Acids Res *48*, 8035-8049. 10.1093/nar/gkaa526.

37. Chevillet, J.R., Kang, Q., Ruf, I.K., Briggs, H.A., Vojtech, L.N., Hughes, S.M., Cheng, H.H., Arroyo, J.D., Meredith, E.K., Gallichotte, E.N., et al. (2014). Quantitative and stoichiometric analysis of the microRNA content of exosomes. Proc Natl Acad Sci U S A *111*, 14888-14893. 10.1073/pnas.1408301111.

38. Bervoets, S., Jacob, M.S., Devineni, A.V., Mahoney, B.D., Sullivan, K.R., Butts, A.R., Sung, H., Einstein, J., Metzstein, M.M., Dus, M., et al. (2024). dArc1 controls sugar reward valuation in Drosophila melanogaster. bioRxiv. 10.1101/2024.11.04.621761.

39. Qi, Y., Wang, J.K., McMillian, M., and Chikaraishi, D.M. (1997). Characterization of a CNS cell line, CAD, in which morphological differentiation is initiated by serum deprivation. J Neurosci *17*, 1217-1225. 10.1523/JNEUROSCI.17-04-01217.1997.

40. Mews, P., Donahue, G., Drake, A.M., Luczak, V., Abel, T., and Berger, S.L. (2017). Acetyl-CoA synthetase regulates histone acetylation and hippocampal memory. Nature *546*, 381-386. 10.1038/nature22405.

41. Wang, H., and Oxford, G.S. (2000). Voltage-dependent ion channels in CAD cells: A catecholaminergic neuronal line that exhibits inducible differentiation. J Neurophysiol *84*, 2888-2895. 10.1152/jn.2000.84.6.2888.

42. Thery, C., Amigorena, S., Raposo, G., and Clayton, A. (2006). Isolation and characterization of exosomes from cell culture supernatants and biological fluids. Curr Protoc Cell Biol *Chapter 3*, Unit 3 22. 10.1002/0471143030.cb0322s30.

43. Kugeratski, F.G., Hodge, K., Lilla, S., McAndrews, K.M., Zhou, X., Hwang, R.F., Zanivan, S., and Kalluri, R. (2021). Quantitative proteomics identifies the core proteome of exosomes with syntenin-1 as the highest abundant protein and a putative universal biomarker. Nat Cell Biol *23*, 631-641. 10.1038/s41556-021-00693-y.

44. Chitti, S.V., Gummadi, S., Kang, T., Shahi, S., Marzan, A.L., Nedeva, C., Sanwlani, R., Bramich, K., Stewart, S., Petrovska, M., et al. (2024). Vesiclepedia 2024: an extracellular vesicles and extracellular particles repository. Nucleic Acids Res *52*, D1694-D1698. 10.1093/nar/gkad1007.

45. You, Y., Zhang, Z., Sultana, N., Ericsson, M., Martens, Y.A., Sun, M., Kanekiyo, T., Ikezu, S., Shaffer, S.A., and Ikezu, T. (2023). ATP1A3 as a target for isolating neuron-specific extracellular vesicles from human brain and biofluids. Sci Adv *9*, eadi3647. 10.1126/sciadv.adi3647.

994 46. Bellingham, S.A., Coleman, B.M., and Hill, A.F. (2012). Small RNA deep sequencing
995 reveals a distinct miRNA signature released in exosomes from prion-infected neuronal
996 cells. Nucleic Acids Res *40*, 10937-10949. 10.1093/nar/gks832.

997 47. Crocker, O.J., Trigg, N.A., and Conine, C.C. (2022). Cloning and Sequencing Eukaryotic
998 Small RNAs. Curr Protoc *2*, e495. 10.1002/cpz1.495.

999 48. Gustafsson, H.T., Ferguson, L., Galan, C., Yu, T., Upton, H., Kaymak, E., Weng, Z.,
1000 Collins, K., and Rando, O.J. (2025). Deep sequencing of yeast and mouse tRNAs and
1001 tRNA fragments using OTTR. Elife *14*. 10.7554/eLife.77616.

1002 49. Scacchetti, A., Shields, E.J., Trigg, N.A., Lee, G.S., Wilusz, J.E., Conine, C.C., and
1003 Bonasio, R. (2024). A ligation-independent sequencing method reveals tRNA-derived
1004 RNAs with blocked 3' termini. Mol Cell *84*, 3843-3859 e3848.
1005 10.1016/j.molcel.2024.07.008.

1006 50. Vilcaes, A.A., Chanaday, N.L., and Kavalali, E.T. (2021). Interneuronal exchange and
1007 functional integration of synaptobrevin via extracellular vesicles. Neuron *109*, 971-983
1008 e975. 10.1016/j.neuron.2021.01.007.

1009 51. Tosar, J.P., Witwer, K., and Cayota, A. (2021). Revisiting Extracellular RNA Release,
1010 Processing, and Function. Trends Biochem Sci *46*, 438-445. 10.1016/j.tibs.2020.12.008.

1011 52. Liu, X.M., Ma, L., and Schekman, R. (2021). Selective sorting of microRNAs into
1012 exosomes by phase-separated YBX1 condensates. Elife *10*. 10.7554/eLife.71982.

1013 53. Sanson, K.R., Hanna, R.E., Hegde, M., Donovan, K.F., Strand, C., Sullender, M.E.,
1014 Vaimberg, E.W., Goodale, A., Root, D.E., Piccioni, F., and Doench, J.G. (2018). Optimized
1015 libraries for CRISPR-Cas9 genetic screens with multiple modalities. Nat Commun *9*, 5416.
1016 10.1038/s41467-018-07901-8.

1017 54. Toribio, V., and Yanez-Mo, M. (2022). Tetraspanins interweave EV secretion, endosomal
1018 network dynamics and cellular metabolism. Eur J Cell Biol *101*, 151229.
1019 10.1016/j.ejcb.2022.151229.

1020 55. Matsui, T., Osaki, F., Hiragi, S., Sakamaki, Y., and Fukuda, M. (2021). ALIX and ceramide
1021 differentially control polarized small extracellular vesicle release from epithelial cells.
1022 EMBO Rep *22*, e51475. 10.15252/embr.202051475.

1023 56. Kunitake, K., Mizuno, T., Hattori, K., Oneyama, C., Kamiya, M., Ota, S., Urano, Y., and
1024 Kojima, R. (2024). Barcoding of small extracellular vesicles with CRISPR-gRNA enables
1025 comprehensive, subpopulation-specific analysis of their biogenesis and release
1026 regulators. Nat Commun *15*, 9777. 10.1038/s41467-024-53736-x.

1027 57. Conibear, E., Cleck, J.N., and Stevens, T.H. (2003). Vps51p mediates the association of
1028 the GARP (Vps52/53/54) complex with the late Golgi t-SNARE Tlg1p. Mol Biol Cell *14*,
1029 1610-1623. 10.1091/mbc.e02-10-0654.

1030 58. Reggiori, F., Wang, C.W., Stromhaug, P.E., Shintani, T., and Klionsky, D.J. (2003). Vps51
1031 is part of the yeast Vps fifty-three tethering complex essential for retrograde traffic from

1032 the early endosome and Cvt vesicle completion. J Biol Chem *278*, 5009-5020.
1033 10.1074/jbc.M210436200.

1034 59. Baietti, M.F., Zhang, Z., Mortier, E., Melchior, A., Degeest, G., Geeraerts, A., Ivarsson, Y.,
1035 Depoortere, F., Coomans, C., Vermeiren, E., et al. (2012). Syndecan-syntenin-ALIX
1036 regulates the biogenesis of exosomes. Nat Cell Biol *14*, 677-685. 10.1038/ncb2502.

1037 60. Henriques, W.S., Young, J.M., Nemudryi, A., Nemudraia, A., Wiedenheft, B., and Malik,
1038 H.S. (2024). The Diverse Evolutionary Histories of Domesticated Metaviral Capsid Genes
1039 in Mammals. Mol Biol Evol *41*. 10.1093/molbev/msae061.

1040 61. Madigan, V., Zhang, Y., Raghavan, R., Wilkinson, M.E., Faure, G., Puccio, E., Segel, M.,
1041 Lash, B., Macrae, R.K., and Zhang, F. (2024). Human paraneoplastic antigen Ma2
1042 (PNMA2) forms icosahedral capsids that can be engineered for mRNA delivery. Proc Natl
1043 Acad Sci U S A *121*, e2307812120. 10.1073/pnas.2307812120.

1044 62. Al Othman, A., Bagrov, D., Rozenberg, J.M., Glazova, O., Skryabin, G., Tchevkina, E.,
1045 Mezentsev, A., and Durymanov, M. (2024). Retrovirus-like gag protein Arc/Arg3.1 is
1046 involved in extracellular-vesicle-mediated mRNA transfer between glioma cells. Biochim
1047 Biophys Acta Gen Subj *1868*, 130522. 10.1016/j.bbagen.2023.130522.

1048 63. Xu, J., Erlendsson, S., Singh, M., Holling, G.A., Regier, M., Ibiricu, I., Einstein, J., Hantak,
1049 M.P., Day, G.S., Piquet, A.L., et al. (2024). PNMA2 forms immunogenic non-enveloped
1050 virus-like capsids associated with paraneoplastic neurological syndrome. Cell *187*, 831-
1051 845 e819. 10.1016/j.cell.2024.01.009.

1052 64. Rintala-Dempsey, A.C., and Kothe, U. (2017). Eukaryotic stand-alone pseudouridine
1053 synthases - RNA modifying enzymes and emerging regulators of gene expression? RNA
1054 Biol *14*, 1185-1196. 10.1080/15476286.2016.1276150.

1055 65. Sun, C., Guo, R., Ye, X., Tang, S., Chen, M., Zhou, P., Yang, M., Liao, C., Li, H., Lin, B.,
1056 et al. (2024). Wybutosine hypomodification of tRNAphe activates HERVK and impairs
1057 neuronal differentiation. iScience *27*, 109748. 10.1016/j.isci.2024.109748.

1058 66. Takakura, M., Ishiguro, K., Akichika, S., Miyauchi, K., and Suzuki, T. (2019). Biogenesis
1059 and functions of aminocarboxypropyluridine in tRNA. Nat Commun *10*, 5542.
1060 10.1038/s41467-019-13525-3.

1061 67. Zhao, X., Ma, D., Ishiguro, K., Saito, H., Akichika, S., Matsuzawa, I., Mito, M., Irie, T.,
1062 Ishibashi, K., Wakabayashi, K., et al. (2023). Glycosylated queuosines in tRNAs optimize
1063 translational rate and post-embryonic growth. Cell *186*, 5517-5535 e5524.
1064 10.1016/j.cell.2023.10.026.

1065 68. Li, J.B., and Walkley, C.R. (2025). Leveraging genetics to understand ADAR1-mediated
1066 RNA editing in health and disease. Nat Rev Genet *26*, 532-546. 10.1038/s41576-025-
1067 00830-5.

1068 69. Rorbach, J., Boesch, P., Gammage, P.A., Nicholls, T.J., Pearce, S.F., Patel, D., Hauser,
1069 A., Perocchi, F., and Minczuk, M. (2014). MRM2 and MRM3 are involved in biogenesis of
1070 the large subunit of the mitochondrial ribosome. Mol Biol Cell *25*, 2542-2555.
1071 10.1091/mbc.E14-01-0014.

1072 70. Rubio Gomez, M.A., and Ibba, M. (2020). Aminoacyl-tRNA synthetases. RNA *26*, 910-
1073 936. 10.1261/rna.071720.119.

1074 71. Kuncha, S.K., Mazeed, M., Singh, R., Kattula, B., Routh, S.B., and Sankaranarayanan, R.
1075 (2018). A chiral selectivity relaxed paralog of DTD for proofreading tRNA mischarging in
1076 Animalia. Nat Commun *9*, 511. 10.1038/s41467-017-02204-w.

1077 72. Ruan, L.L., Zhou, X.L., Tan, M., and Wang, E.D. (2013). Human cytoplasmic ProX edits
1078 mischarged tRNAPro with amino acid but not tRNA specificity. Biochem J *450*, 243-252.
1079 10.1042/BJ20121493.

1080 73. Caudron-Herger, M., Jansen, R.E., Wassmer, E., and Diederichs, S. (2021). RBP2GO: a
1081 comprehensive pan-species database on RNA-binding proteins, their interactions and
1082 functions. Nucleic Acids Res *49*, D425-D436. 10.1093/nar/gkaa1040.

1083 74. Herridge, R.P., Dolata, J., Migliori, V., de Santis Alves, C., Borges, F., Schorn, A.J., van
1084 Ex, F., Lin, A., Bajczyk, M., Parent, J.S., et al. (2025). Pseudouridine guides germline
1085 small RNA transport and epigenetic inheritance. Nat Struct Mol Biol *32*, 277-286.
1086 10.1038/s41594-024-01392-6.

1087 75. Kampmann, M. (2018). CRISPRi and CRISPRa Screens in Mammalian Cells for Precision
1088 Biology and Medicine. ACS Chem Biol *13*, 406-416. 10.1021/acschembio.7b00657.

1089 76. Dai, Q., Zhang, L.S., Sun, H.L., Pajdzik, K., Yang, L., Ye, C., Ju, C.W., Liu, S., Wang, Y.,
1090 Zheng, Z., et al. (2023). Quantitative sequencing using BID-seq uncovers abundant
1091 pseudouridines in mammalian mRNA at base resolution. Nat Biotechnol *41*, 344-354.
1092 10.1038/s41587-022-01505-w.

1093 77. Schwartz, S., Bernstein, D.A., Mumbach, M.R., Jovanovic, M., Herbst, R.H., Leon-
1094 Ricardo, B.X., Engreitz, J.M., Guttman, M., Satija, R., Lander, E.S., et al. (2014).
1095 Transcriptome-wide mapping reveals widespread dynamic-regulated pseudouridylation of
1096 ncRNA and mRNA. Cell *159*, 148-162. 10.1016/j.cell.2014.08.028.

1097 78. Trigg, N.A., and Conine, C.C. (2024). Epididymal acquired sperm microRNAs modify post-
1098 fertilization embryonic gene expression. Cell Rep *43*, 114698.
1099 10.1016/j.celrep.2024.114698.

1100 79. Brito, C., and Sousa, S. (2020). Non-Muscle Myosin 2A (NM2A): Structure, Regulation
1101 and Function. Cells *9*. 10.3390/cells9071590.

1102 80. Caudron-Herger, M., Rusin, S.F., Adamo, M.E., Seiler, J., Schmid, V.K., Barreau, E.,
1103 Kettenbach, A.N., and Diederichs, S. (2019). R-DeeP: Proteome-wide and Quantitative
1104 Identification of RNA-Dependent Proteins by Density Gradient Ultracentrifugation. Mol
1105 Cell *75*, 184-199 e110. 10.1016/j.molcel.2019.04.018.

1106 81. Lu, A., Wawro, P., Morgens, D.W., Portela, F., Bassik, M.C., and Pfeffer, S.R. (2018).
1107 Genome-wide interrogation of extracellular vesicle biology using barcoded miRNAs. Elife
1108 *7*. 10.7554/eLife.41460.

1109 82. Dixson, A.C., Dawson, T.R., Di Vizio, D., and Weaver, A.M. (2023). Context-specific
1110 regulation of extracellular vesicle biogenesis and cargo selection. Nat Rev Mol Cell Biol
1111 *24*, 454-476. 10.1038/s41580-023-00576-0.

1112 83. Korkut, C., Ataman, B., Ramachandran, P., Ashley, J., Barria, R., Gherbesi, N., and
1113 Budnik, V. (2009). Trans-synaptic transmission of vesicular Wnt signals through
1114 Evi/Wntless. Cell *139*, 393-404. 10.1016/j.cell.2009.07.051.

1115 84. Blanchette, C.R., Scalera, A.L., Harris, K.P., Zhao, Z., Dresselhaus, E.C., Koles, K., Yeh,
1116 A., Apiki, J.K., Stewart, B.A., and Rodal, A.A. (2022). Local regulation of extracellular
1117 vesicle traffic by the synaptic endocytic machinery. J Cell Biol *221*.
1118 10.1083/jcb.202112094.

1119 85. Erlendsson, S., Morado, D.R., Cullen, H.B., Feschotte, C., Shepherd, J.D., and Briggs,
1120 J.A.G. (2020). Structures of virus-like capsids formed by the Drosophila neuronal Arc
1121 proteins. Nat Neurosci *23*, 172-175. 10.1038/s41593-019-0569-y.

1122 86. Sullivan, K.R., Ravens, A., Walker, A.C., and Shepherd, J.D. (2025). "Arc - A viral vector
1123 of memory and synaptic plasticity". Curr Opin Neurobiol *91*, 102979.
1124 10.1016/j.conb.2025.102979.

1125 87. Whiteley, A.M., and Shepherd, J.D. (2026). Retrotransposons unplugged: Rewiring the
1126 nervous system and wreaking havoc. Neuron *114*, 33-45. 10.1016/j.neuron.2025.09.034.

1127 88. Cerneckis, J., Cui, Q., He, C., Yi, C., and Shi, Y. (2022). Decoding pseudouridine: an
1128 emerging target for therapeutic development. Trends Pharmacol Sci *43*, 522-535.
1129 10.1016/j.tips.2022.03.008.

1130 89. Qu, S., Nelson, H.M., Liu, X., Wang, Y., Semler, E.M., Michell, D.L., Massick, C., Franklin,
1131 J.L., Karijolich, J., Weaver, A.M., et al. (2024). 5-Fluorouracil treatment represses
1132 pseudouridine-containing miRNA export into extracellular vesicles. J Extracell Biol *3*,
1133 e70010. 10.1002/jex2.70010.

1134 90. Wei, S., Dai, X., Yuan, J., He, S., Shah, K., Guo, S., Duan, Z., Murn, J., and Wang, Y.
1135 (2025). Quantitative Proteomics Identifies Profilin-1 as a Pseudouridine-Binding Protein.
1136 J Am Chem Soc *147*, 1458-1462. 10.1021/jacs.4c17659.

1137 91. Holliday, L.S., Faria, L.P., and Rody, W.J., Jr. (2019). Actin and Actin-Associated Proteins
1138 in Extracellular Vesicles Shed by Osteoclasts. Int J Mol Sci *21*. 10.3390/ijms21010158.

1139 92. Grosshans, H., Lecointe, F., Grosjean, H., Hurt, E., and Simos, G. (2001). Pus1p-
1140 dependent tRNA pseudouridinylation becomes essential when tRNA biogenesis is
1141 compromised in yeast. J Biol Chem *276*, 46333-46339. 10.1074/jbc.M107141200.

1142 93. Patton, J.R., Bykhovskaya, Y., Mengesha, E., Bertolotto, C., and Fischel-Ghodsian, N.
1143 (2005). Mitochondrial myopathy and sideroblastic anemia (MLASA): missense mutation in
1144 the pseudouridine synthase 1 (PUS1) gene is associated with the loss of tRNA
1145 pseudouridylation. J Biol Chem *280*, 19823-19828. 10.1074/jbc.M500216200.

1146 94. Xie, Y., Chai, P., Till, N.A., Hemberger, H., Lebedenko, C.G., Porat, J., Watkins, C.P.,
1147 Caldwell, R.M., George, B.M., Perr, J., et al. (2024). The modified RNA base acp(3)U is

1148 an attachment site for N-glycans in glycoRNA. Cell *187*, 5228-5237 e5212.
1149 10.1016/j.cell.2024.07.044.

1150 95. Sharma, S., Jiao, X., Yang, J., Kwan, K.Y., and Kiledjian, M. (2025). Extracellular
1151 exosomal RNAs are glyco-modified. Nature Cell Biology *27*, 983-991. 10.1038/s41556-
1152 025-01682-1.

1153 96. Ma, L., Lu, H., Tian, Z., Yang, M., Ma, J., Shang, G., Liu, Y., Xie, M., Wang, G., Wu, W.,
1154 et al. (2022). Structural insights into the interactions and epigenetic functions of human
1155 nucleic acid repair protein ALKBH6. J Biol Chem *298*, 101671. 10.1016/j.jbc.2022.101671.

1156 97. Chen, Z., Zhou, Y., Xue, C., Zeng, L., Deng, S., Xu, Z., Li, M., Zhao, H., He, X., Liu, S., et
1157 al. (2025). Psychological stress-induced ALKBH5 deficiency promotes tumour innervation
1158 and pancreatic cancer via extracellular vesicle transfer of RNA. Nat Cell Biol *27*, 1035-
1159 1047. 10.1038/s41556-025-01667-0.

1160 98. Barman, B., Sung, B.H., Krystofiak, E., Ping, J., Ramirez, M., Millis, B., Allen, R., Prasad,
1161 N., Chetyrkin, S., Calcutt, M.W., et al. (2022). VAP-A and its binding partner CERT drive
1162 biogenesis of RNA-containing extracellular vesicles at ER membrane contact sites. Dev
1163 Cell *57*, 974-994 e978. 10.1016/j.devcel.2022.03.012.

1164 99. Caohuy, H., and Pollard, H.B. (2002). Protein kinase C and guanosine triphosphate
1165 combine to potentiate calcium-dependent membrane fusion driven by annexin 7. J Biol
1166 Chem *277*, 25217-25225. 10.1074/jbc.M202452200.

1167 100. Tartaglia, G.G., Hollas, H., Havik, B., Vedeler, A., and Pastore, A. (2025). The RNA-
1168 Binding Properties of Annexins. J Mol Biol *437*, 168933. 10.1016/j.jmb.2024.168933.

1169 101. Sonder, S.L., Boye, T.L., Tolle, R., Dengjel, J., Maeda, K., Jaattela, M., Simonsen, A.C.,
1170 Jaiswal, J.K., and Nylandsted, J. (2019). Annexin A7 is required for ESCRT III-mediated
1171 plasma membrane repair. Sci Rep *9*, 6726. 10.1038/s41598-019-43143-4.

1172 102. Cafe, S.L., Anderson, A.L., and Nixon, B. (2020). In vitro Induction and Detection of
1173 Acrosomal Exocytosis in Human Spermatozoa. Bio Protoc *10*, e3689.
1174 10.21769/BioProtoc.3689.

1175 103. Doench, J.G., Fusi, N., Sullender, M., Hegde, M., Vaimberg, E.W., Donovan, K.F., Smith,
1176 I., Tothova, Z., Wilen, C., Orchard, R., et al. (2016). Optimized sgRNA design to maximize
1177 activity and minimize off-target effects of CRISPR-Cas9. Nat Biotechnol *34*, 184-191.
1178 10.1038/nbt.3437.

1179 104. Shalem, O., Sanjana, N.E., Hartenian, E., Shi, X., Scott, D.A., Mikkelson, T., Heckl, D.,
1180 Ebert, B.L., Root, D.E., Doench, J.G., and Zhang, F. (2014). Genome-scale CRISPR-Cas9
1181 knockout screening in human cells. Science *343*, 84-87. 10.1126/science.1247005.

1182 105. Ahlmann-Eltze, C., and Anders, S. (2020). proDA: Probabilistic Dropout Analysis for
1183 Identifying Differentially Abundant Proteins in Label-Free Mass Spectrometry. biorXiv.
1184 10.1101/661496.

1185 106. Kammers, K., Cole, R.N., Tiengwe, C., and Ruczinski, I. (2015). Detecting Significant
1186 Changes in Protein Abundance. EuPA Open Proteom *7*, 11-19.
1187 10.1016/j.euprot.2015.02.002.

1188 107. Ritchie, M.E., Phipson, B., Wu, D., Hu, Y., Law, C.W., Shi, W., and Smyth, G.K. (2015).
1189 limma powers differential expression analyses for RNA-sequencing and microarray
1190 studies. Nucleic Acids Res *43*, e47. 10.1093/nar/gkv007.

1191 108. Huang, D.W., Sherman, B.T., and Lempicki, R.A. (2008). Systematic and integrative
1192 analysis of large gene lists using DAVID bioinformatics resources. Nature Protocols *4*, 44-
1193 57. 10.1038/nprot.2008.211.

1194 109. Sherman, B.T., Hao, M., Qiu, J., Jiao, X., Baseler, M.W., Lane, H.C., Imamichi, T., and
1195 Chang, W. (2022). DAVID: a web server for functional enrichment analysis and functional
1196 annotation of gene lists (2021 update). Nucleic Acids Res *50*, W216-W221.
1197 10.1093/nar/gkac194.

1198 110. Dobin, A., Davis, C.A., Schlesinger, F., Drenkow, J., Zaleski, C., Jha, S., Batut, P.,
1199 Chaisson, M., and Gingeras, T.R. (2013). STAR: ultrafast universal RNA-seq aligner.
1200 Bioinformatics *29*, 15-21. 10.1093/bioinformatics/bts635.

1201 111. Zhang, Y., Parmigiani, G., and Johnson, W.E. (2020). ComBat-seq: batch effect
1202 adjustment for RNA-seq count data. NAR Genom Bioinform *2*, lqaa078.
1203 10.1093/nargab/lqaa078.

1204 112. Martin, M. (2011). Cutadapt removes adapter sequences from high-throughput
1205 sequencing reads. EMBnet.journal *17*. 10.14806/ej.17.1.200.

1206 113. Langmead, B., and Salzberg, S.L. (2012). Fast gapped-read alignment with Bowtie 2. Nat
1207 Methods *9*, 357-359. 10.1038/nmeth.1923.

1208 114. Smith, T., Heger, A., and Sudbery, I. (2017). UMI-tools: modeling sequencing errors in
1209 Unique Molecular Identifiers to improve quantification accuracy. Genome Res *27*, 491-
1210 499. 10.1101/gr.209601.116.

1211 115. Quinlan, A.R. (2014). BEDTools: The Swiss-Army Tool for Genome Feature Analysis. Curr
1212 Protoc Bioinformatics *47*, 11 12 11-34. 10.1002/0471250953.bi1112s47.

1213 116. Li, W., Xu, H., Xiao, T., Cong, L., Love, M.I., Zhang, F., Irizarry, R.A., Liu, J.S., Brown, M.,
1214 and Liu, X.S. (2014). MAGeCK enables robust identification of essential genes from
1215 genome-scale CRISPR/Cas9 knockout screens. Genome Biol *15*, 554. 10.1186/s13059-
1216 014-0554-4.

1217 117. Love, M.I., Huber, W., and Anders, S. (2014). Moderated estimation of fold change and
1218 dispersion for RNA-seq data with DESeq2. Genome Biol *15*, 550. 10.1186/s13059-014-
1219 0550-8.

1220 118. Lawrence, M., Huber, W., Pages, H., Aboyoun, P., Carlson, M., Gentleman, R., Morgan,
1221 M.T., and Carey, V.J. (2013). Software for computing and annotating genomic ranges.
1222 PLoS Comput Biol *9*, e1003118. 10.1371/journal.pcbi.1003118.

1223 **FIGURE LEGENDS**

1224 **Figure 1. CADs and primary neurons produce EVs enriched in tRNAs and snoRNAs**

1225 (A) Scheme of EV purification protocol. Conditioned medium was collected and subjected to
1226 several round of centrifugation at increasing speeds to remove cells, cell debris, and large
1227 vesicles. In the last step EVs were pelleted via ultracentrifugation at 100,000 x *g*.

1228 (B) Nanoparticle tracking analysis of EVs from CADs. The plot shows the average ($n = 2$) number
1229 of particles per mL on the *y* axis and their size on the *x* axis. The vertical dashed line indicates
1230 the median size.

1231 (C) Comparison of cellular and EV proteomes by mass spectrometry. Gray, significantly different
1232 proteins (adjusted $p < 0.1$; $n = 2$); blue, EV markers; yellow, cellular markers.

1233 (D) Gel electrophoresis (2% agarose-formaldehyde) comparing cellular *vs.* EV RNA. Individual
1234 replicates were loaded in separate lanes.

1235 (E) RNA content of CADs EVs *vs.* cells, measured by deep sequencing (LIDAR). Red, transcripts
1236 significantly enriched in EVs [exRNAs; adjusted $p < 0.1$ and $\log_2$(EVs/cells) > 0; $n \geq 3$].

1237 (F) Same as (E) with different classes of RNA highlighted by colors, as indicated.

1238 (G) Left: EVs were incubated with RNase A/T1 to digest all RNAs not protected by a lipid bilayer.
1239 Right: enrichment of exRNAs (EVs vs. cells) in EVs from CADs before (x axis) and after (y axis)
1240 RNase treatment. Only exRNAs significantly different (adjusted $p < 0.1$) in either treatment are
1241 shown. $\rho$, Spearman's correlation value.

1242 (H–I) Same as (E–F) but for EVs purified by size-exclusion chromatography from cultured rat
1243 primary neurons ($n = 2$).

1244 **Figure 2. A genome-wide screen identifies regulators of RNA secretion**

1245 (A) Scheme of the genetic screen. CADs were transduced with a lentiviral library containing
1246 sgRNAs against most protein coding genes. Two (baseline) and 10 (readout) days later, cells and
1247 EVs were harvested to measure sgRNA levels.

1248 (B) Hypothetical gene categories with expected changes in sgRNA abundance over time in cells
1249 and EVs.

1250 (C) Change in sgRNA abundance ($n$ = 4 sgRNAs per gene), compared to their average
1251 abundance in the corresponding sample (cells or EVs) at day 2. Individual biological replicates
1252 (r1 and r2) are shown.

1253 (D) Observed/predicted ratio of sgRNAs targeting putative positive (left) and negative (right)
1254 regulators of RNA secretion, derived from MaGECK analysis. Significant hits ($p < 0.05$) are in red
1255 ($n = 2$). Candidates mentioned in the text are highlighted in blue.

1256 (E) GO analysis (cellular component) of significant positive regulators from (D).

1257 (F) Predicted (gray) vs. observed (red) sgRNA abundances in EVs (± SEM), normalized to the
1258 average predicted abundance (see methods), for retrovirus-derived proteins identified as
1259 significant ($p < 0.05$) positive regulators from MaGECK analysis. Values for individual sgRNAs
1260 are shown.

1261 (G) Same as (F) but for RNA-modifying enzymes.

1262 **Figure 3. PUS1 facilitates the export of select exRNAs**

1263 (A) Western blot probing for PUS1, SDCBP, and β-TUB (control) in wild type (WT) and 2 different
1264 *Pus1*$^{-/-}$ CAD clones.

1265 (B) Differences in exRNA abundance between wild type and *Pus1*$^{-/-}$, as measured by LIDAR. Red,
1266 transcripts showing significant difference ($n \geq 3$, adjusted $p < 0.1$).

1267 (C) Overlap between RNAs less abundant ("DOWN") in *Pus1*$^{-/-}$ cells compared to WT, either inside
1268 the cells (gray, "cellular") or inside EVs (red, "extracellular").

1269 (D) Ratios of RNA abundance in EVs and inside cells comparing wild type (blue) and *Pus1*$^{-/-}$ (gold)
1270 CADs. Average and distributions are shown by the boxes and individual transcripts are shown in
1271 points. RNAs were divided in the indicated classes and the $p$ values were obtained with Student's
1272 $t$ tests. Data from ≥ 3 biological replicates.

1273 (E) Scheme showing the different types of known tRNA-derived RNAs (tDRs).

1274 (F) Changes in full-length tRNAs or tDRs between wild type and *Pus1*$^{-/-}$ in cells (grey) or EVs (red).
1275 $P$ values are from a Wilcoxon rank sum test. Data from ≥ 3 biological replicates.

1276 **Figure 4. Ψ selects RNAs for secretion**

1277 (A) Scheme of the Ψ sequencing approach. Bisulfite-induced deletions were detected with a
1278 modified LIDAR protocol which utilizes $MnCl_2$ during reverse transcription.

1279 (B) Distribution of Ψ-modified RNAs among different classes in CADs and EVs. Data from 2
1280 biological replicates.

1281 (C) Ψ levels, inferred by the % of reads containing a deletion at the corresponding sites, for CAD
1282 cellular RNAs (gray) and exRNAs (red). *P* value is from a Wilcoxon rank sum test.

1283 (D) Same as (C) but for rat primary neurons and corresponding EVs purified by size-exclusion
1284 chromatography.

1285 (E) Top: Schematic representation of the mouse epididymis, highlighting the region of tissue and
1286 EVs used for our analysis (cauda). The direction of sperm movement is indicated by the arrow.
1287 Bottom: Same as (C) but for cauda tissue and corresponding EVs.

1288 (F) Scheme of the sufficiency experiments shown in (G) and (H). CADs were transfected with
1289 RNAs containing only Ψ or U at uridine positions for 6 hours. Their abundance inside and outside
1290 cells was measured 24 hours later by RT-qPCR (G) or sequencing (H).

1291 (G) Abundance of U- (gray) or Ψ-containing (yellow) RNAs 24 hours after transfection inside and
1292 outside CADs, measured by RT-qPCR. *P* values are from Student's *t* tests.

1293 (H) Export ratio ($CPM_{cells}$ / $CPM_{medium}$) for U- (gray) or Ψ-containing (yellow) RNAs, 24 hours after
1294 transfection into CADs. Six distinct sequences were tested, indicated by the numbers 1–6. *P*
1295 values are from Student's *t* tests.

1296 **Figure 5. PUS1 marks RNAs for extracellular export**

1297 (A) Levels of Ψ modification (% of total reads) at individual exRNA sites in wild type (*x* axis) vs.
1298 *Pus1*$^{-/-}$ (*y* axis) CAD EVs. PUS1-sensitive sites, where Ψ was reduced in *Pus1*$^{-/-}$ EVs by at least
1299 25%, are in gold. Other Ψ sites are in gray. Data from 2 biological replicates.

1300 (B) Ratio of the abundance of Ψ-containing RNAs in *Pus1*$^{-/-}$ CAD vs. WT cells (left) or EVs (right).
1301 The RNAs were classified as PUS1-independent (gray, "others") and PUS1-sensitive (gold). Only
1302 RNAs with at least one Ψ site detected in the EV fraction were considered. *P* values are from
1303 Wilcoxon rank sum tests.

1304 (C) % of molecules containing Ψ at the indicated bases according to bisulfite-LIDAR for four
1305 example tRNAs in EVs from wild type (WT) and *Pus1*$^{-/-}$ CAD.

1306 (D) Abundance ($\log_2$-converted, DEseq2 normalized counts) for the full-length tRNAs in (C) in
1307 wild type (gray) or *Pus1*$^{-/-}$ (red) EVs. Asterisks indicate $p < 0.05$ (calculated by DEseq2).

1308 (E–F) Same as (C) and (D) but for the two indicated snoRNAs.

1309 **Figure 6. Extracellular export of Ψ-containing RNAs requires MYL6**

1310 (A) Comparison of protein abundance in the interactome of U- or Ψ-containing RNA, as measured
1311 by mass spectrometry. Dark grey, significantly different proteins (adjusted $p < 0.1$; $n = 2$).

1312 (B) Relative export ratio [export ratio(Ψ) / export ratio(U)] between U- and Ψ-containing RNAs in
1313 the medium from CADs, treated with siRNAs against *Myl6* and control. The different RNA
1314 sequences are identified by the same numbers as in (Fig. 4H). Bars show the mean ± SEM. *P*
1315 values are from Student's *t* tests.

1316 (C) Ratio of the abundance of RNAs in *Myl6* knockdown (KD) vs. control in cells (left), EVs
1317 (middle) or EVs treated with RNase A/T1 (right). The RNAs were classified as U-containing (gray,
1318 "others") and Ψ-containing (blue). Only RNAs with at least one Ψ site detected in EVs were
1319 considered. *P* values are from Wilcoxon rank sum tests.

1320 (D) Differences in exRNA abundance (in EVs treated with RNase A/T1) between control and *Myl6*
1321 knockdown (KD) as measured by LIDAR. Red, transcripts showing significant difference (adjusted
1322 $p < 0.1$; $n \geq 2$).

1323 (E) Proposed model for exRNA secretion. PUS1 marks specific RNAs with Ψ to select them as
1324 exRNAs. Once deposited, Ψ provides a binding site for MYL6, which routes RNAs into EVs
1325 formed via multivesicular bodies or by direct plasma membrane budding.

1326 **SUPPLEMENTARY FIGURE LEGENDS**

1327 **Figure S1. Additional analyses on exRNAs contained in EVs**

1328 (A) Overlap between the CAD EV proteome (see Fig. 1C) and proteins in the Vesiclepedia
1329 database (Kitti et al., 2024). The *p* value is from a hypergeometric test.

1330 (B) Top 9 enriched GO terms ("cellular component" aspect) associated with proteins significantly
1331 enriched in EVs from Fig. 1C.

1332 (C) RNA class distribution as % of transcripts significantly (adjusted $p < 0.1$) enriched in cells
1333 compared to EVs and *vice versa*.

1334 (D) Distribution of average ($n \geq 3$) log-fold-changes between cells and EVs for C/D box and H/ACA
1335 box snoRNAs.

1336 (E) Average ($n \geq 3$) insert size distribution of reads mapping to tRNAs in cells and EVs.

1337 (F) Average ($n \geq 3$) tRNA and tDR distribution in cells and EVs.

1338 (G) RNAs from EVs subjected to RNase A/T1 digestion in the absence or presence of 1% Triton
1339 X-100 were resolved on a 2% agarose-formaldehyde gel. Two amounts of RNaseA/T1 mix were
1340 used (++, 2 µg RNase A and 5 U RNase T1 per reaction; +, 0.2 µg RNase A and 0.5 U RNase
1341 T1). Cellular RNA (lane 1) and RNA extracted from untreated EVs (lane 2) were loaded as
1342 controls.

1343 (H) Nanoparticle tracking analysis of EVs purified by size-exclusion chromatography from primary
1344 rat neuron cultures. The number of particles per mL is plotted on the *y* axis and their size on the
1345 *x* axis. The vertical dashed line indicates the median size.

1346 **Figure S2. Analyses and validations on the genome-wide screen for exRNAs**

1347 (A) RT-qPCR for sgRNA abundance (expressed as ratio to *Rpl32* RNA) in cells and EVs from
1348 sgRNA-expressing CAD and controls.

1349 (B) Scheme of the logic underpinning the genome-wide screen. A fraction of sgRNAs expressed
1350 from a U6 promoter enter endogenous secretion pathways, for example by being loaded into
1351 intraluminal vesicles of multivesicular bodies (MVBs, derived from endosomal maturation) or
1352 directly by budding from the plasma membrane. This allows for the genotype of the originating
1353 cell to be determined via the sgRNA content of the EVs.

1354 (C) Scheme of the LIDAR adaptation used to directly sequence the sgRNAs from the EVs.

1355 (D) Number of sgRNAs that were detected (yellow) or not (blue) in cells and EV in each screen
1356 replicate. Individual samples are shown. Horizontal dashed line indicates the 95% of all sgRNAs
1357 included in the library.

1358 (E) Comparison of the abundance of all individual sgRNAs inside cells vs. EVs at day 2 after
1359 transduction. Red, sgRNAs with significant difference ($n$ = 2, adjusted $p$ < 0.1).

1360 (F) Nucleotide representation at individual CRISPR RNA (crRNA) targeting sequence positions
1361 for all, preferentially exported, and preferentially retained sgRNAs. The bracket indicates the first
1362 3 positions, enriched for Us in the exported sgRNAs.

1363 (G) Average predicted (gray) and observed (red) values (± SEM) for sgRNAs targeting *Sdcbp.*
1364 Circles represent values for the individual sgRNAs.

1365 (H) Western blot for SDCBP and SUZ12 (control) in wild type and 2 different *Sdcbp*$^{-/-}$ CAD clones.

1366 (I) Nanoparticle tracking analysis of EVs isolated from wild type and *Sdcbp*$^{-/-}$ CADs. The plot
1367 shows the number of particles normalized to the number of starting cells on the y axis and their
1368 size on the x axis.

1369 (J) Average particles/cells (± SEM), secreted by wild type and 2 different *Sdcbp*$^{-/-}$ CAD clones ($n$
1370 = 3). Individual replicates are shown.

1371 (K) *Z* score-converted mRNA abundance (normalized DEseq2 counts) for the domesticated
1372 retroviral genes showed in Fig. 2F, before ("CAD") and after ("dCAD") CAD cell differentiation into
1373 a more mature neuronal form.

1374 **Figure S3. Validation of *Pus1* and analyses on exRNAs from *Pus1*$^{-/-}$ cells**

1375 (A) Scheme of secondary CRISPRi screen. Stable CADs, transduced with different CRISPRi
1376 sgRNAs were mixed in equal numbers. Then, the abundance of sgRNAs in the pooled cells and
1377 in the tissue culture medium (extracellular) was measured by LIDAR.

1378 (B) Export rate of the indicated CRISPRi sgRNAs, calculated as a ratio of extracellular over
1379 intercellular abundance. "Scr." denotes sgRNA scrambled control. *P* values are from Student's *t*
1380 tests.

1381 (C) Differences in cellular RNA abundance between wild type and *Pus1*$^{-/-}$, as measured by LIDAR.
1382 Red, transcripts showing significant difference ($n$ ≥ 3, adjusted $p$ < 0.1).

1383 (D) Overlap between RNAs more abundant ("UP") in *Pus1*$^{-/-}$ cells compared to WT, either inside
1384 the cells (gray, "cellular") or in EVs (red, "extracellular").

1385 (E) Correlations in the change in RNA abundance between wild type and *Pus1*$^{-/-}$ CADs (*x axis*)
1386 and EVs (*y* axis) for the RNAs significantly changed (adjusted $p < 0.1$) in either set. Spearman's
1387 correlation values are reported.

1388 **Figure S4. Validation of Ψ sequencing**

1389 (A) LIDAR read densities (normalized to counts per millions) for individual nucleotides of an *in*
1390 *vitro*-transcribed Ψ-containing RNA. Top, input; bottom, BID-treated.

1391 (B) Inferred % of Ψ based on % of deletion in LIDAR reads mapping to 18s rRNA from CAD RNA.
1392 Top, input; bottom, BID-treated.

1393 (C–D) Overlap between Ψ-containing RNAs (C) or individual sites (D) identified in CADs and EVs.
1394 *P* values are from hypergeometric tests.

1395 (E) Denaturing agarose-formaldehyde (2%) electrophoresis of total tissue (cellular) and EV RNA
1396 from cauda epididymis (individual replicates are shown).

1397 **Figure S5. Analyses on exRNAs from *Pus1*$^{-/-}$ CADs**

1398 (A) Distribution of transcripts containing PUS1-sensitive Ψ sites in CADs and EVs among the
1399 indicated RNA classes. Data from 2 biological replicates.

1400 (B) Distribution of reads containing PUS1-sensitive Ψ sites and mapping to tRNAs genes among
1401 the indicated types of tRNA-derived species in cells and EVs.

1402 (C) % of Ψ modification detected at each canonical tRNA position in wild type or *Pus1*$^{-/-}$ CAD EVs.
1403 Data from the two different *Pus1*$^{-/-}$ clones are shown separately.

1404 (D) % of Ψ at every canonical tRNA position (column) for every tRNA iso-acceptor containing a
1405 U at position 27 (rows) in EVs from wild type (left) or *Pus1*$^{-/-}$ (right) CADs.

1406 (E) Scheme of canonical Ψ sites on tRNAs. In blue, Ψ sites dependent on PUS1.

1407 (F) Overlap between significantly reduced full-length tRNAs in *Pus1*$^{-/-}$ (red) and PUS1 full-length
1408 tRNA targets (yellow) in EVs. *P* value is from a hypergeometric test.

1409 (G) Same as (F) but for snoRNAs. For all panels data were from two biological replicates. In the
1410 case of *Pus1*$^{-/-}$ the two individual knockout clones were used as combined replicates.

1411 For all panels data were from two biological replicates. In the case of *Pus1*$^{-/-}$ the two individual
1412 knockout clones were used as combined replicates ($n = 2$ per clone).

1413 **Figure S6. Additional analyses for MYL6**

1414 (A) IP/beads values for U- and Ψ-RNAs interactomes measured by mass spectrometry. In red,
1415 significantly different proteins (adjusted $p < 0.1$; $n = 2$).

1416 (B) MYL6 protein abundance in CADs and EVs. Individual replicates are shown.

1417 (C) Average predicted (gray) and observed (red) values (± SEM) for sgRNAs targeting *Myl6.*
1418 Circles represent individual sgRNAs. The *p* value is from MaGECK analysis.

1419 (D) *Myl6* mRNA abundance relative to control (*Rpl32*). Bars show average ± SEM. Individual
1420 replicates are shown. *P* values are from a Student's t test

1421 (E) Differences in intracellular RNA abundance between control and *Myl6* knockdown (KD) as
1422 measured by LIDAR. Red, transcripts showing significant difference (adjusted $p < 0.1$; $n \geq 2$).

1423 (F) Same as (E) but for RNAs contained in EVs.

1424 **SUPPLEMENTARY TABLE LEGENDS**

1425 **Table S1. Proteomics of CADs and EVs**

1426 **Table S2. Genome-wide screen results**

1427 **Table S3. RNA-binding proteins within positive regulators of exRNA biogenesis**

1428 **Table S4. Proteomics results from U- and Ψ-containing RNA pulldowns**

1429 **Table S5. Oligonucleotides used in this study**

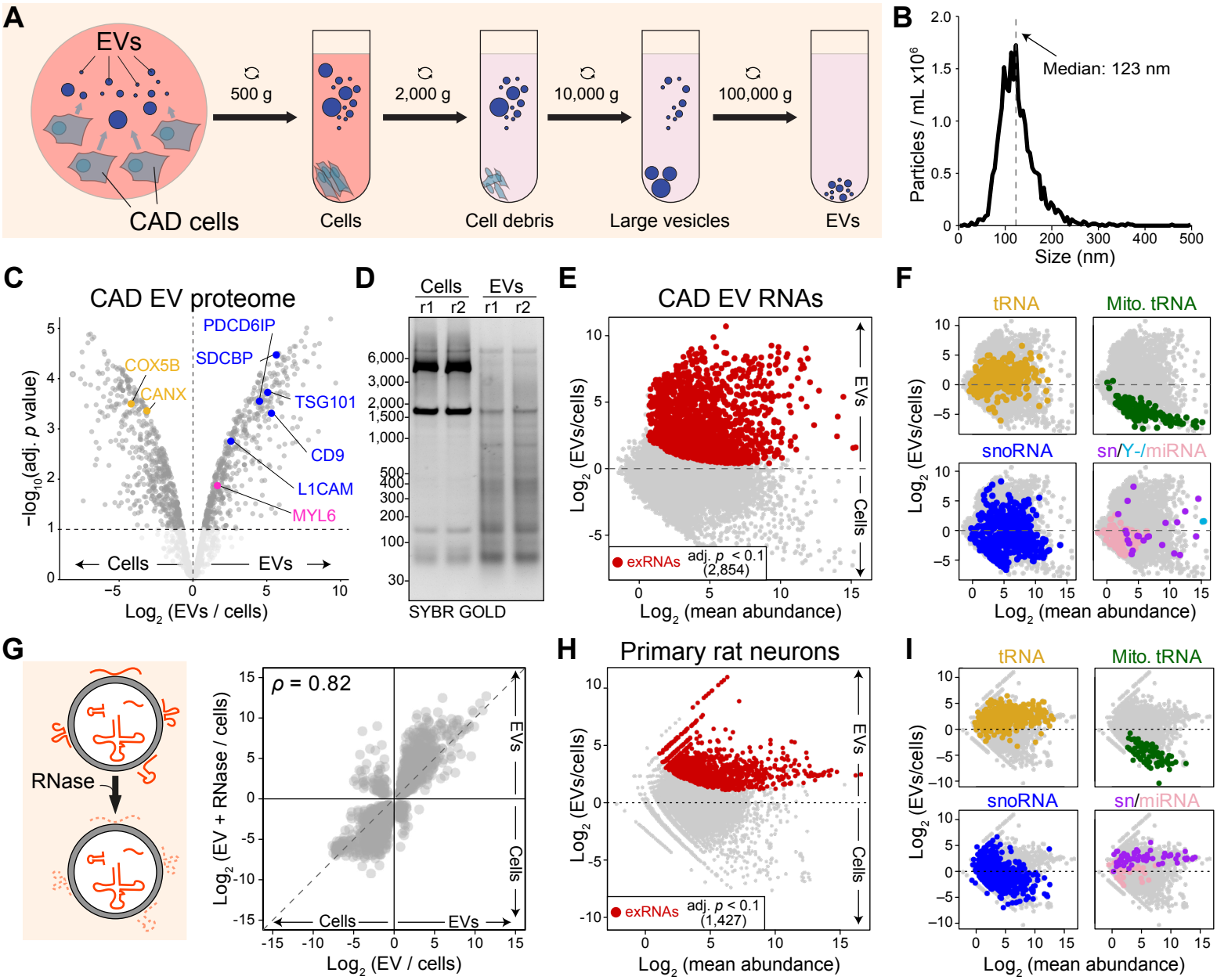


**Figure 1. CADs and primary neurons produce EVs enriched in tRNAs and snoRNAs**

(A) Scheme of EV purification protocol. Conditioned medium was collected and subjected to several round of centrifugation at increasing speeds to remove cells, cell debris, and large vesicles. In the last step EVs were pelleted via ultracentrifugation at 100,000 x *g*.

(B) Nanoparticle tracking analysis of EVs from CADs. The plot shows the average (n = 2) number of particles per mL on the y axis and their size on the x axis. The vertical dashed line indicates the median size.

(C) Comparison of cellular and EV proteomes by mass spectrometry. Gray, significantly different proteins (adjusted p < 0.1; n = 2); blue, EV markers; yellow, cellular markers.

(D) Gel electrophoresis (2% agarose-formaldehyde) comparing cellular vs. EV RNA. Individual replicates were loaded in separate lanes.

(E) RNA content of CADs EVs vs. cells, measured by deep sequencing (LIDAR). Red, transcripts significantly enriched in EVs [exRNAs; adjusted $p < 0.1$ and $\log_2$(EVs/cells) > 0; $n \geq 3$].

(F) Same as (E) with different classes of RNA highlighted by colors, as indicated.

(G) Left: EVs were incubated with RNase A/T1 to digest all RNAs not protected by a lipid bilayer. Right: enrichment of exRNAs (EVs vs. cells) in EVs from CADs before (*x* axis) and after (*y* axis) RNase treatment. Only exRNAs significantly different (adjusted $p < 0.1$) in either treatment are shown. $\rho$, Spearman's correlation value.

(H–I) Same as (E–F) but for EVs purified by size-exclusion chromatography from cultured rat primary neurons (n = 2).

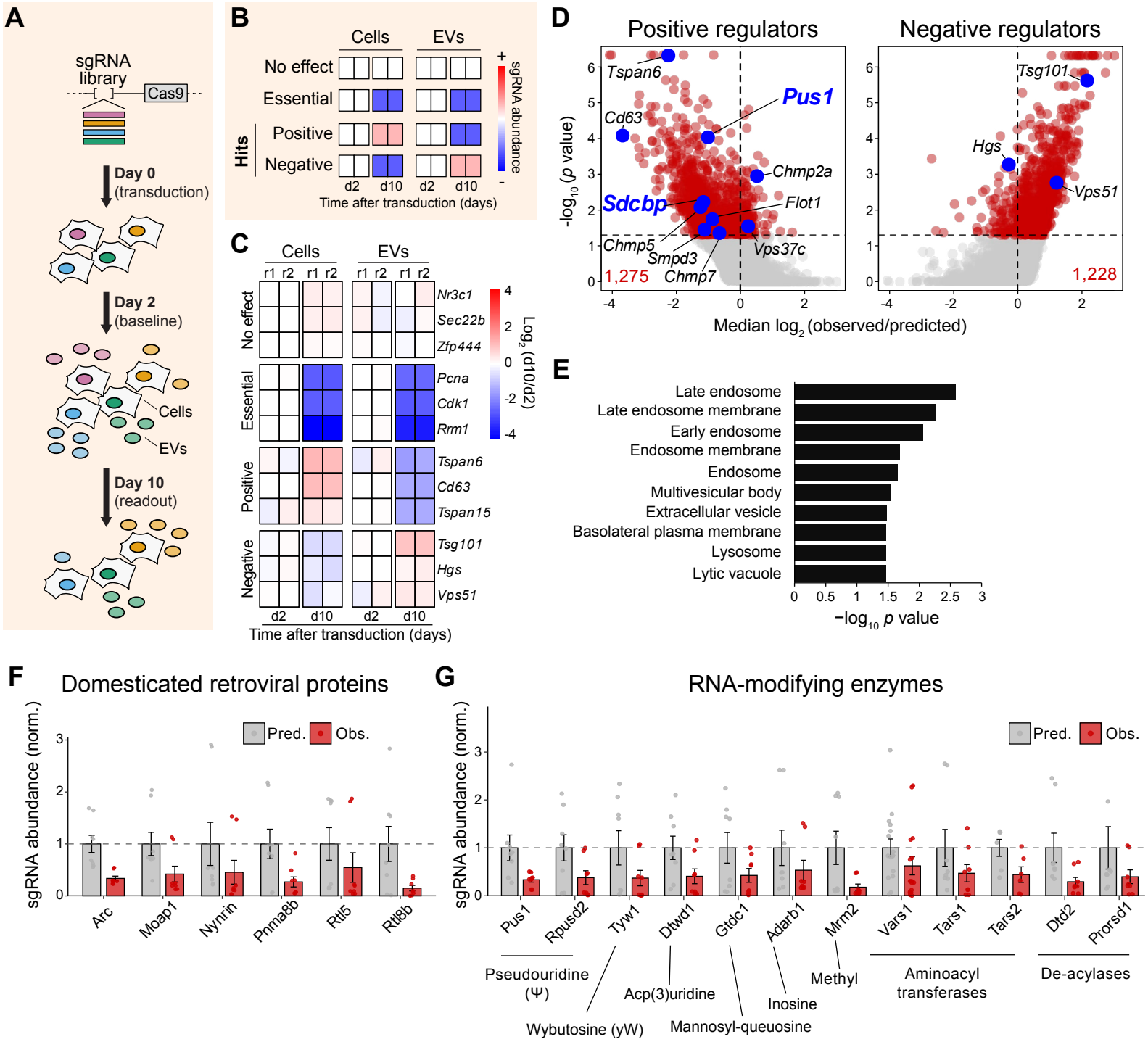


**Figure 2. A genome-wide screen identifies regulators of RNA secretion**

(A) Scheme of the genetic screen. CADs were transduced with a lentiviral library containing sgRNAs against most protein coding genes. Two (baseline) and 10 (readout) days later, cells and EVs were harvested to measure sgRNA levels.

(B) Hypothetical gene categories with expected changes in sgRNA abundance over time in cells and EVs.

(C) Change in sgRNA abundance (n = 4 sgRNAs per gene), compared to their average abundance in the corresponding sample (cells or EVs) at day 2. Individual biological replicates (r1 and r2) are shown.

(D) Observed/predicted ratio of sgRNAs targeting putative positive (left) and negative (right) regulators of RNA secretion, derived from MaGECK analysis. Significant hits (p value < 0.05) are in red (n = 2). Candidates mentioned in the text are highlighted in blue.

(E) GO analysis (cellular component) of significant positive regulators from (D).

(F) Predicted (gray) vs. observed (red) sgRNA abundances in EVs ( SEM), normalized to the average predicted abundance (see methods), for retrovirus-derived proteins identified as significant (p < 0.05) positive regulators from MaGECK analysis. Values for individual sgRNAs are shown.

(G) Same as (F) but for RNA-modifying enzymes.

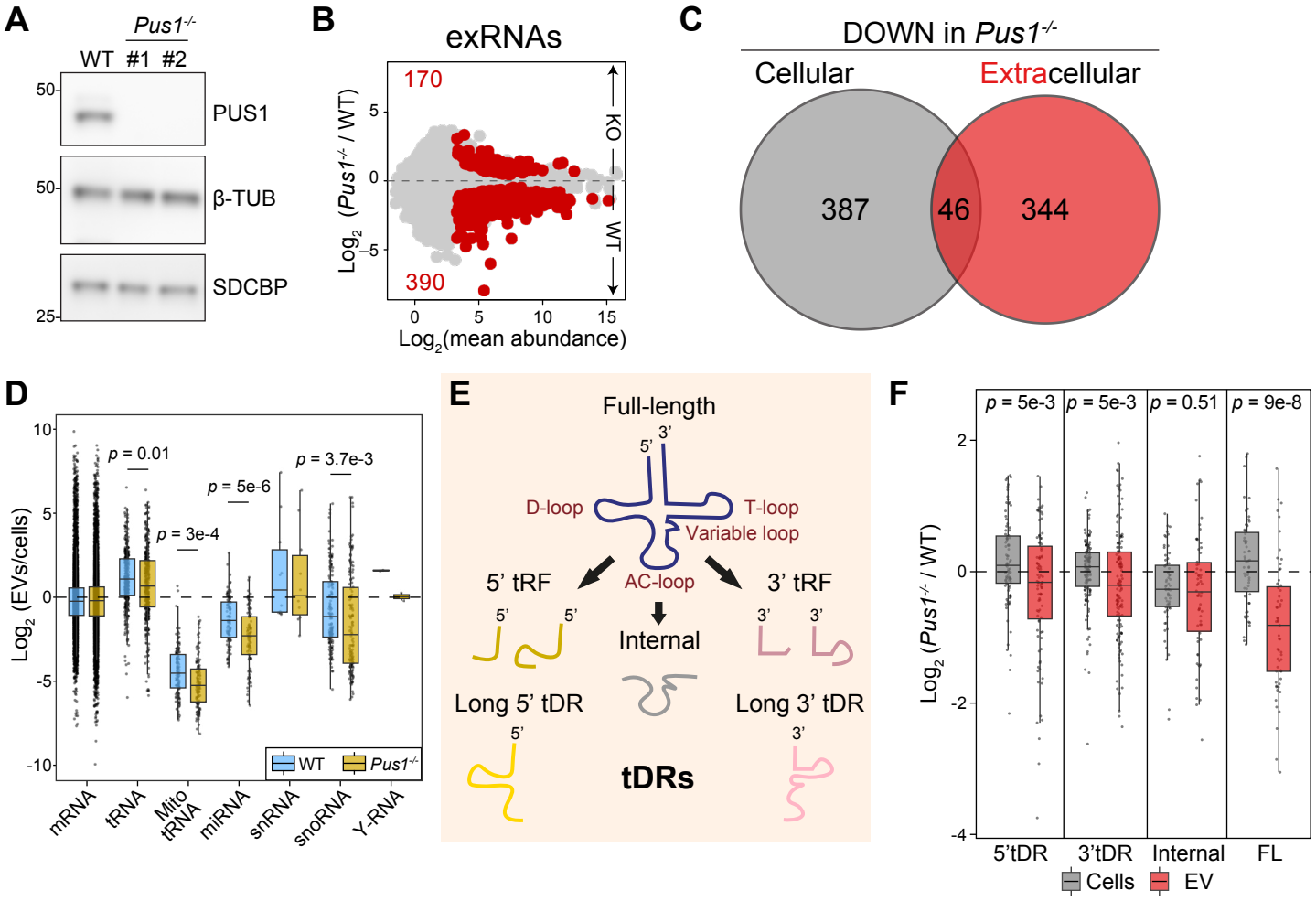


**Figure 3. PUS1 facilitates the export of select exRNAs**

(A) Western blot probing for PUS1, SDCBP, and β-TUB (control) in wild type (WT) and 2 different Pus1-/- CAD clones.

(B) Differences in exRNA abundance between wild type and Pus1-/-, as measured by LIDAR. Red, transcripts showing significant difference (n ≥ 3, adjusted p < 0.1).

(C) Overlap between RNAs less abundant ("DOWN") in Pus1-/- cells compared to WT, either inside the cells (gray, "cellular") or inside EVs (red, "extracellular").

(D) Ratios of RNA abundance in EVs and inside cells comparing wild type (blue) and Pus1-/- (gold) CADs. Average and distributions are shown by the boxes and individual transcripts are shown in points. RNAs were divided in the indicated classes and the p values were obtained with Student's t tests. Data from ≥ 3 biological replicates.

(E) Scheme showing the different types of known tRNA-derived RNAs (tDRs).

(F) Changes in full-length tRNAs or tDRs between wild type and Pus1-/- in cells (grey) or EVs (red). P values are from a Wilcoxon rank sum test. Data from ≥ 3 biological replicates.

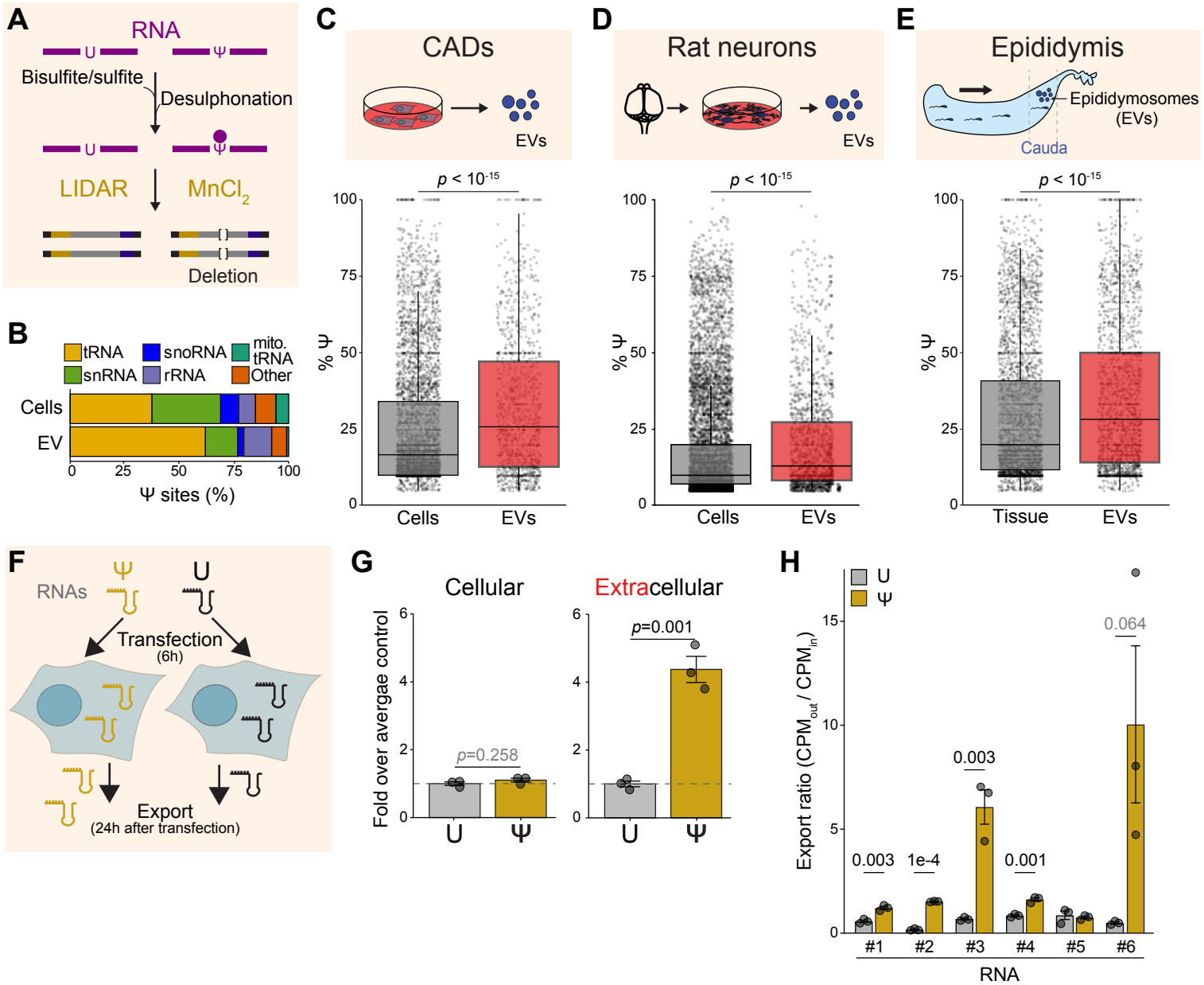


**Figure 4. Ψ selects RNAs for secretion**

(A) Scheme of the Ψ sequencing approach. Bisulfite-induced deletions were detected with a modified LIDAR protocol which utilizes $MnCl_2$ during reverse transcription.

(B) Distribution of Ψ-modified RNAs among different classes in CADs and EVs. Data from 2 biological replicates.

(C) Ψ levels, inferred by the % of reads containing a deletion at the corresponding sites, for CAD cellular RNAs (gray) and exRNAs (red). P value is from a Wilcoxon rank sum test.

(D) Same as (C) but for rat primary neurons and corresponding EVs purified by size-exclusion chromatography.

(E) Top: Schematic representation of the mouse epididymis, highlighting the region of tissue and EVs used for our analysis (cauda). The direction of sperm movement is indicated by the arrow. Bottom: Same as (C) but for cauda tissue and corresponding EVs.

(F) Scheme of the sufficiency experiments shown in (G) and (H). CADs were transfected with RNAs containing only Ψ or U at uridine positions for 6 hours. Their abundance inside and outside cells was measured 24 hours later by RT-qPCR (G) or sequencing (H).

(G) Abundance of U- (gray) or Ψ-containing (yellow) RNAs 24 hours after transfection inside and outside CADs, measured by RT-qPCR. P values are from Student's t tests.

(H) Export ratio (CPMcells / CPMmedium) for U- (gray) or Ψ-containing (yellow) RNAs, 24 hours after transfection into CADs. Six distinct sequences were tested, indicated by the numbers 1–6. P values are from Student's t tests.

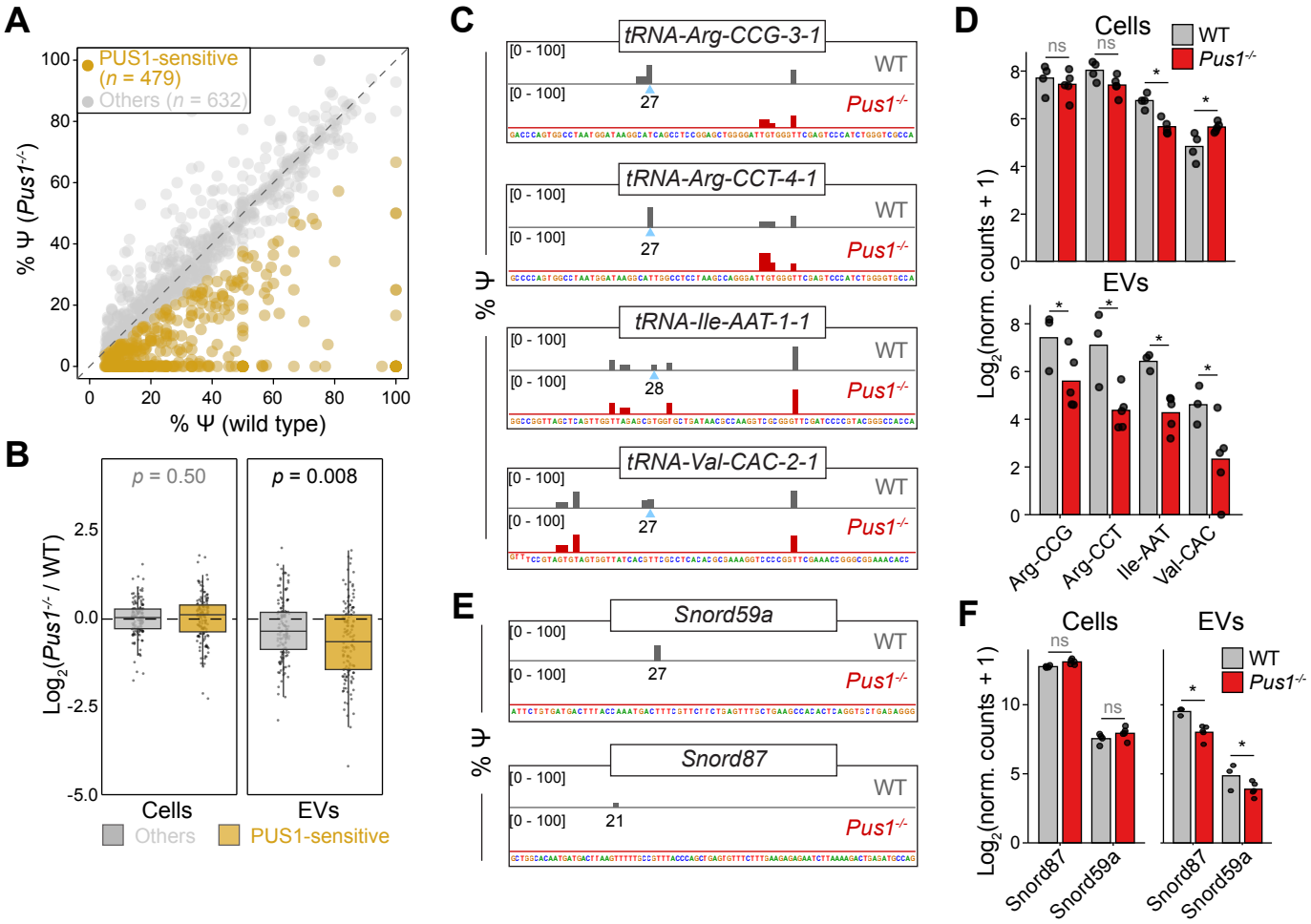


**Figure 5. PUS1 marks RNAs for extracellular export**

(A) Levels of Ψ modification (% of total reads) at individual exRNA sites in wild type (x axis) vs. Pus1-/- (y axis) CAD EVs. PUS1-sensitive sites, where Ψ was reduced in Pus1-/- EVs by at least 25%, are in gold. Other Ψ sites are in gray. Data from 2 biological replicates.

(B) Ratio of the abundance of Ψ-containing RNAs in Pus1-/- CAD vs. WT cells (left) or EVs (right). The RNAs were classified as PUS1-independent (gray, "others") and PUS1-sensitive (gold). Only RNAs with at least one Ψ site detected in the EV fraction were considered. P values are from Wilcoxon rank sum tests.

(C) % of molecules containing Ψ at the indicated bases according to bisulfite-LIDAR for four example tRNAs in EVs from wild type (WT) and Pus1-/- CAD.

(D) Abundance (log2-converted, DEseq2 normalized counts) for the full-length tRNAs in (C) in wild type (gray) or Pus1-/- (red) EVs. Asterisks indicate $p < 0.05$ (calculated by DEseq2).

(E–F) Same as (C) and (D) but for the two indicated snoRNAs.

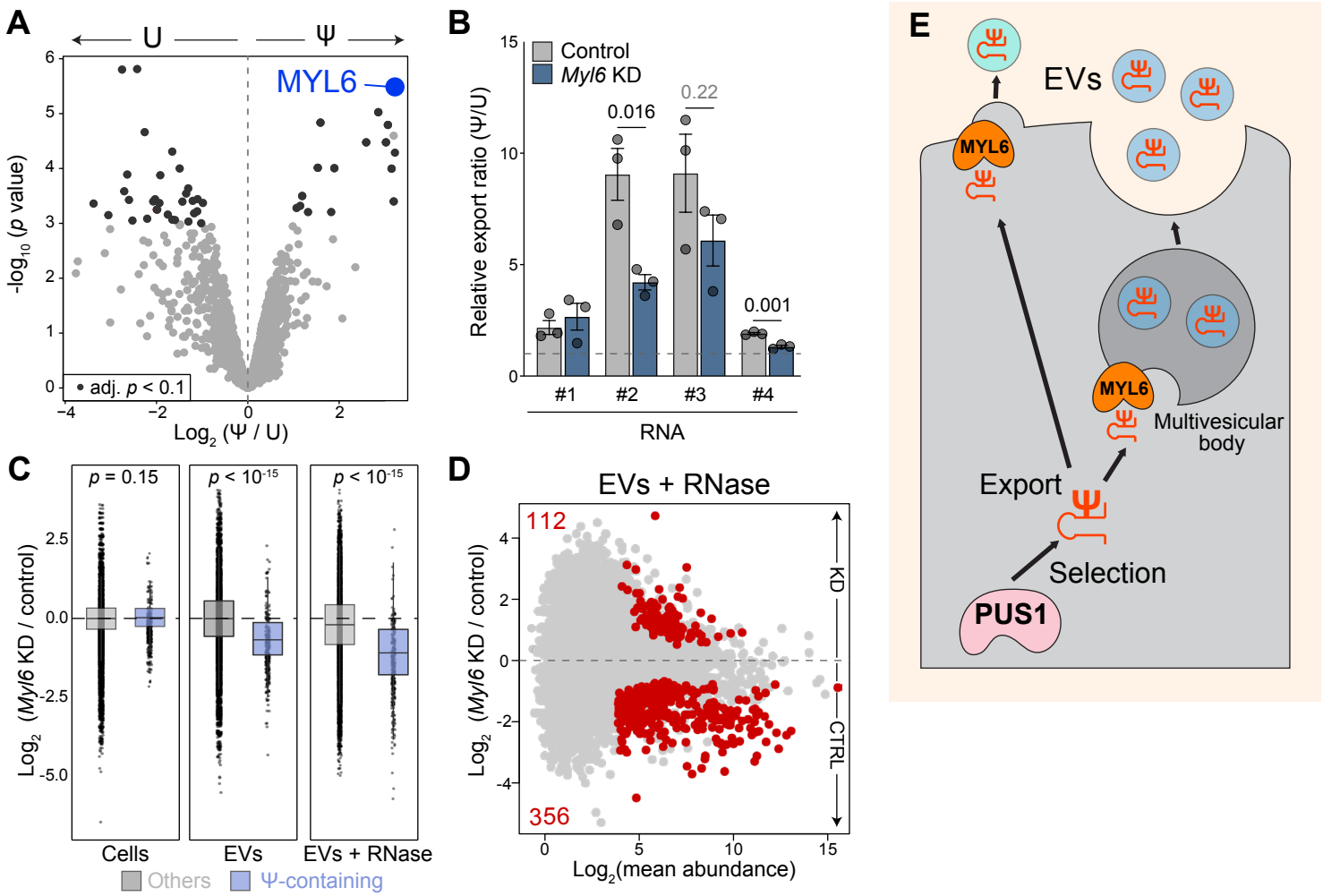


**Figure 6. Extracellular export of Ψ-containing RNAs requires MYL6**

(A) Comparison of protein abundance in the interactome of U- or Ψ-containing RNA, as measured by mass spectrometry. Dark grey, significantly different proteins (adjusted p < 0.1; n = 2).

(B) Relative export ratio [export ratio(Ψ) / export ratio(U)] between U- and Ψ-containing RNAs in the medium from CADs, treated with siRNAs against Myl6 and control. The different RNA sequences are identified by the same numbers as in (Fig. 4H). Bars show the mean ± SEM. P values are from Student's t tests.

(C) Ratio of the abundance of RNAs in Myl6 knockdown (KD) vs. control in cells (left), EVs (middle) or EVs treated with RNase A/T1 (right). The RNAs were classified as U-containing (gray, "others") and Ψ-containing (blue). Only RNAs with at least one Ψ site detected in EVs were considered. P values are from Wilcoxon rank sum tests.

(D) Differences in exRNA abundance (in EVs treated with RNase A/T1) between control and Myl6 knockdown (KD) as measured by LIDAR. Red, transcripts showing significant difference (adjusted p < 0.1; n ≥ 2).

(E) Proposed model for exRNA secretion. PUS1 marks specific RNAs with Ψ to select them as exRNAs. Once deposited, Ψ provides a binding site for MYL6, which routes RNAs into EVs formed via multivesicular bodies or by direct plasma membrane budding.

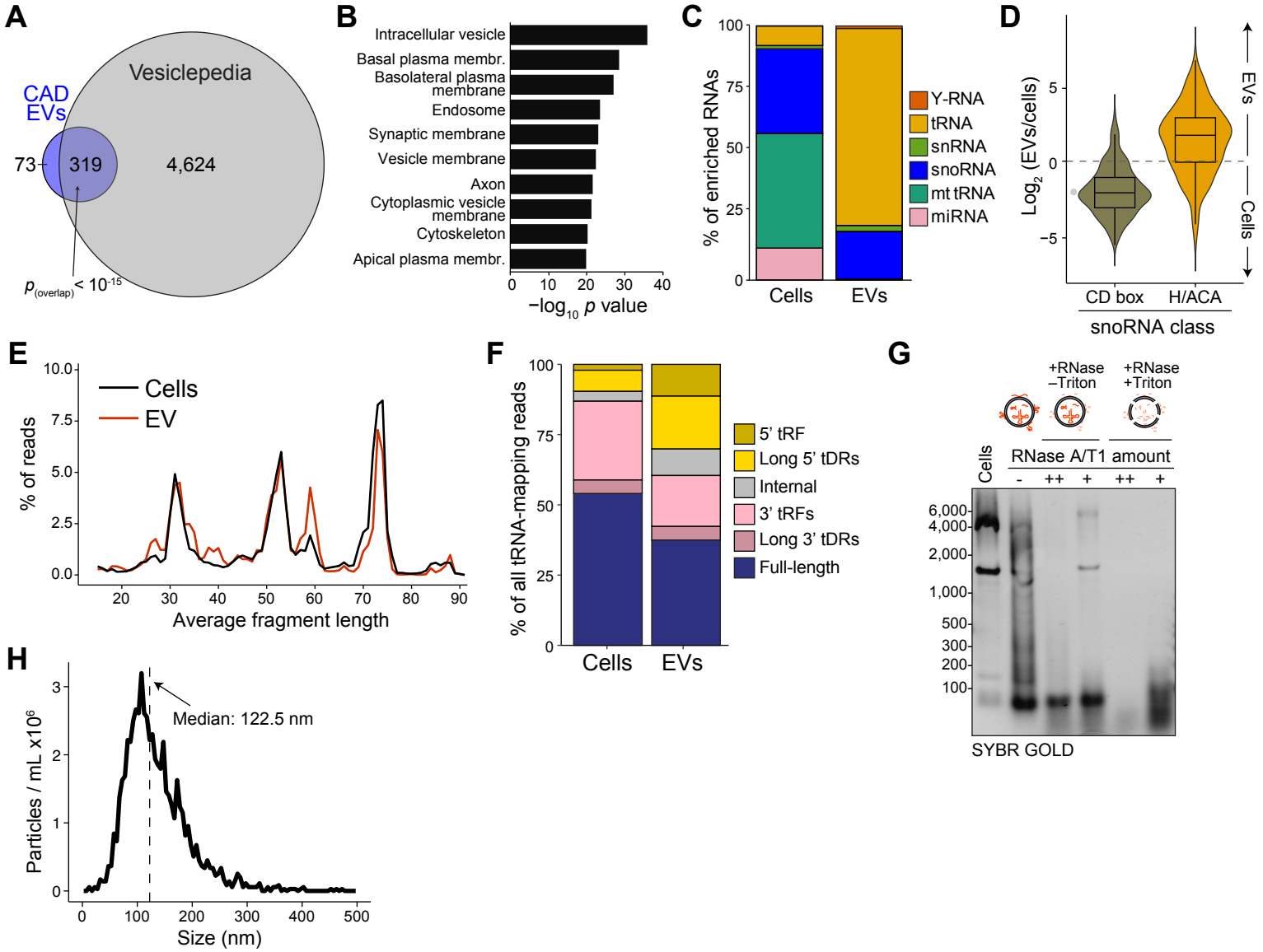


**Figure S1. Additional analyses on exRNAs contained in EVs from CADs**

(A) Overlap between the CAD EV proteome (see Fig. 1C) and proteins in the Vesiclepedia database (Kitti et al., 2024). The p value is from a hypergeometric test.

(B) Top 9 enriched GO terms ("cellular component" aspect) associated with proteins significantly enriched in EVs from Fig. 1C.

(C) RNA class distribution as % of transcripts significantly (adjusted $p < 0.1$) enriched in cells compared to EVs and vice versa.

(D) Distribution of average ($n \geq 3$) log-fold-changes between cells and EVs for C/D box and H/ACA box snoRNAs.

(E) Average ($n \geq 3$) insert size distribution of reads mapping to tRNAs in cells and EVs.

(F) Average ($n \geq 3$) tRNA and tDR distribution in cells and EVs.

(G) RNAs from EVs subjected to RNase A/T1 digestion in the absence or presence of 1% Triton X-100 were resolved on a 2% agarose-formaldehyde gel. Two amounts of RNaseA/T1 mix were used (++, 2 µg RNase A and 5 U RNase T1 per reaction; +, 0.2 µg RNase A and 0.5 U RNase T1). Cellular RNA (lane 1) and RNA extracted from untreated EVs (lane 2) were loaded as controls.

(H) Nanoparticle tracking analysis of EVs purified by size-exclusion chromatography from primary rat neuron cultures. The number of particles per mL is plotted on the y axis and their size on the x axis. The vertical dashed line indicates the median size.

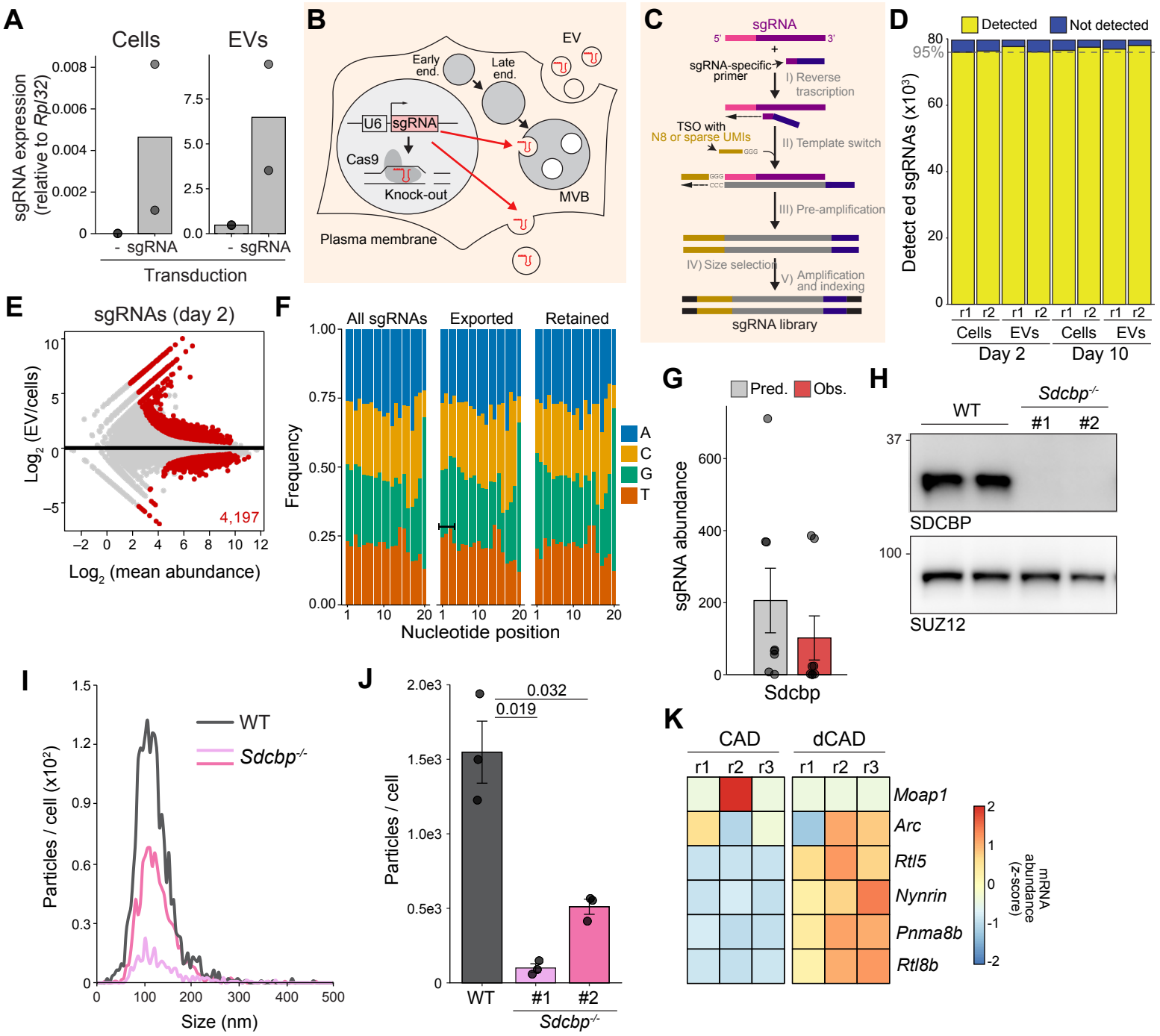


**Figure S2. Analyses and validations on the genome-wide screen for exRNAs**

(A) RT-qPCR for sgRNA abundance (expressed as ratio to Rpl32 RNA) in cells and EVs from sgRNA-expressing CAD and controls.

(B) Scheme of the logic underpinning the genome-wide screen. A fraction of sgRNAs expressed from a U6 promoter enter endogenous secretion pathways, for example by being loaded into intraluminal vesicles of multivesicular bodies (MVBs, derived from endosomal maturation) or directly by budding from the plasma membrane. This allows for the genotype of the originating cell to be determined via the sgRNA content of the EVs.

(C) Scheme of the LIDAR adaptation used to directly sequence the sgRNAs from the EVs.

(D) Number of sgRNAs that were detected (yellow) or not (blue) in cells and EV in each screen replicate. Individual samples are shown. Horizontal dashed line indicates the 95% of all sgRNAs included in the library.

(E) Comparison of the abundance of all individual sgRNAs inside cells vs. EVs at day 2 after transduction. Red, sgRNAs with significant difference (n = 2, adjusted p < 0.1).

(F) Nucleotide representation at individual CRISPR RNA (crRNA) targeting sequence positions for all, preferentially exported, and preferentially retained sgRNAs. The bracket indicates the first 3 positions, enriched for Us in the exported sgRNAs.

(G) Average predicted (gray) and observed (red) values (± SEM) for sgRNAs targeting Sdcbp. Circles represent values for the individual sgRNAs.

(H) Western blot for SDCBP and SUZ12 (control) in wild type and 2 different Sdcbp-/- CAD clones.

(I) Nanoparticle tracking analysis of EVs isolated from wild type and Sdcbp-/- CADs. The plot shows the number of particles normalized to the number of starting cells on the y axis and their size on the x axis.

(J) Average particles/cells (± SEM), secreted by wild type and 2 different Sdcbp-/- CAD clones (n = 3). Individual replicates are shown.

(K) Z score-converted mRNA abundance (normalized DEseq2 counts) for the domesticated retroviral genes showed in Fig. 2F, before ("CAD") and after ("dCAD") CAD cell differentiation into a more mature neuronal form.

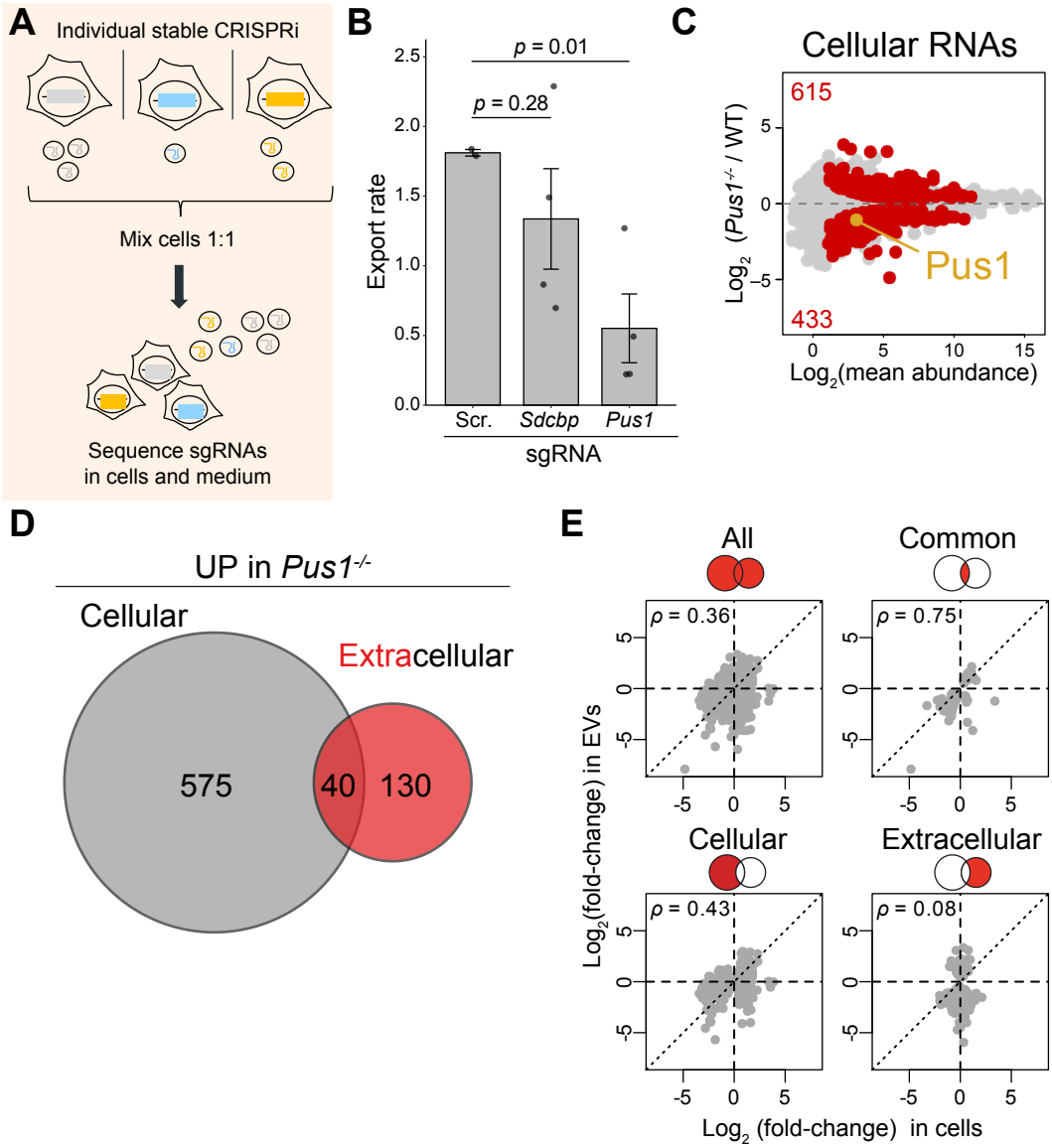


**Figure S3. Validation of *Pus1* and analyses on exRNAs from *Pus1*$^{-/-}$ cells**

(A) Scheme of secondary CRISPRi screen. Stable CADs, transduced with different CRISPRi sgRNAs were mixed in equal numbers. Then, the abundance of sgRNAs in the pooled cells and in the tissue culture medium (extracellular) was measured by LIDAR.

(B) Export rate of the indicated CRISPRi sgRNAs, calculated as a ratio of extracellular over intercellular abundance. “Scr.” denotes sgRNA scrambled control. P values are from Student’s t tests.

(C) Differences in cellular RNA abundance between wild type and Pus1-/-, as measured by LIDAR. Red, transcripts showing significant difference ($n \geq 3$, adjusted $p < 0.1$).

(D) Overlap between RNAs more abundant (“UP”) in Pus1-/- cells compared to WT, either inside the cells (gray, “cellular”) or in EVs (red, “extracellular”).

(E) Correlations in the change in RNA abundance between wild type and Pus1-/- CADs (x axis) and EVs (y axis) for the RNAs significantly changed (adjusted $p < 0.1$) in either set. Spearman’s correlation values are reported.

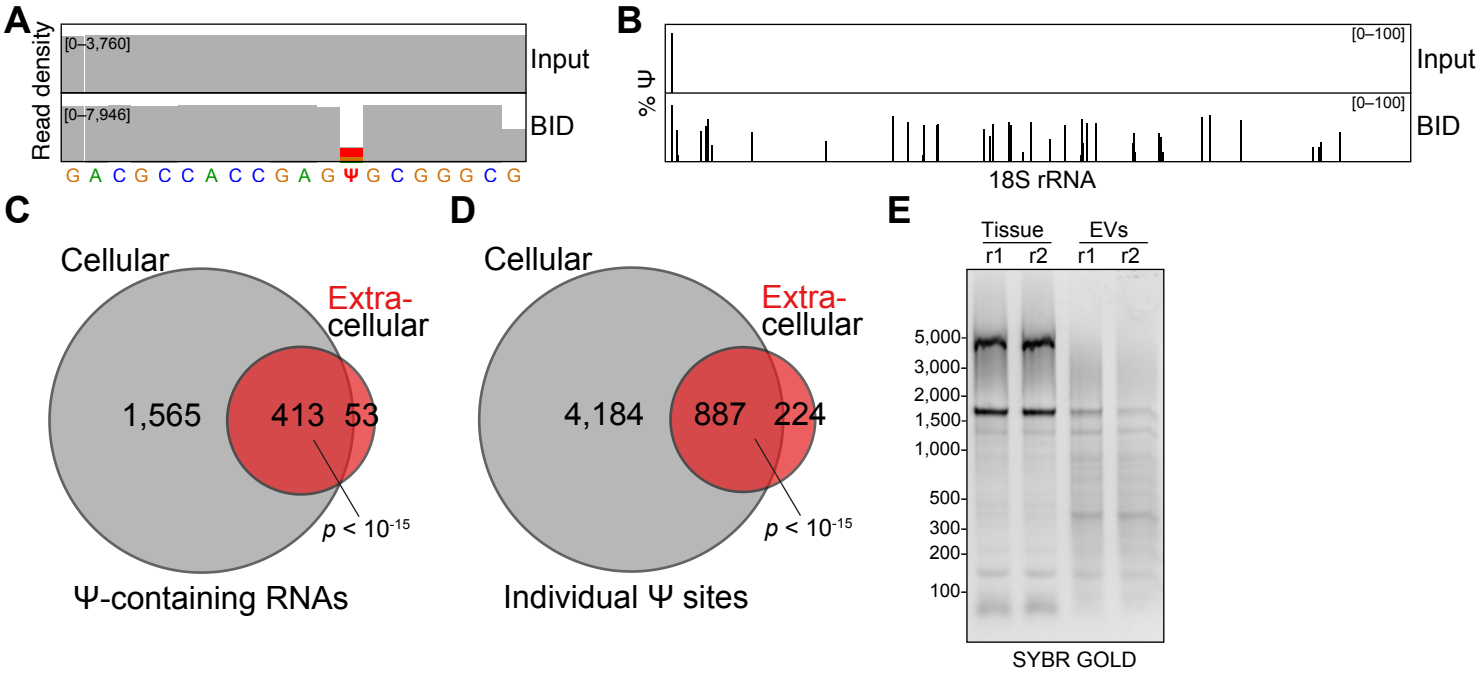


**Figure S4. Validation of Ψ sequencing**

(A) LIDAR read densities (normalized to counts per millions) for individual nucleotides of an in vitro-transcribed Ψ-containing RNA. Top, input; bottom, BID-treated.

(B) Inferred % of Ψ based on % of deletion in LIDAR reads mapping to 18s rRNA from CAD RNA. Top, input; bottom, BID-treated.

(C–D) Overlap between Ψ-containing RNAs (C) or individual sites (D) identified in CADs and EVs. P values are from hypergeometric tests.

(E) Denaturing agarose-formaldehyde (2%) electrophoresis of total tissue (cellular) and EV RNA from cauda epididymis (individual replicates are shown).

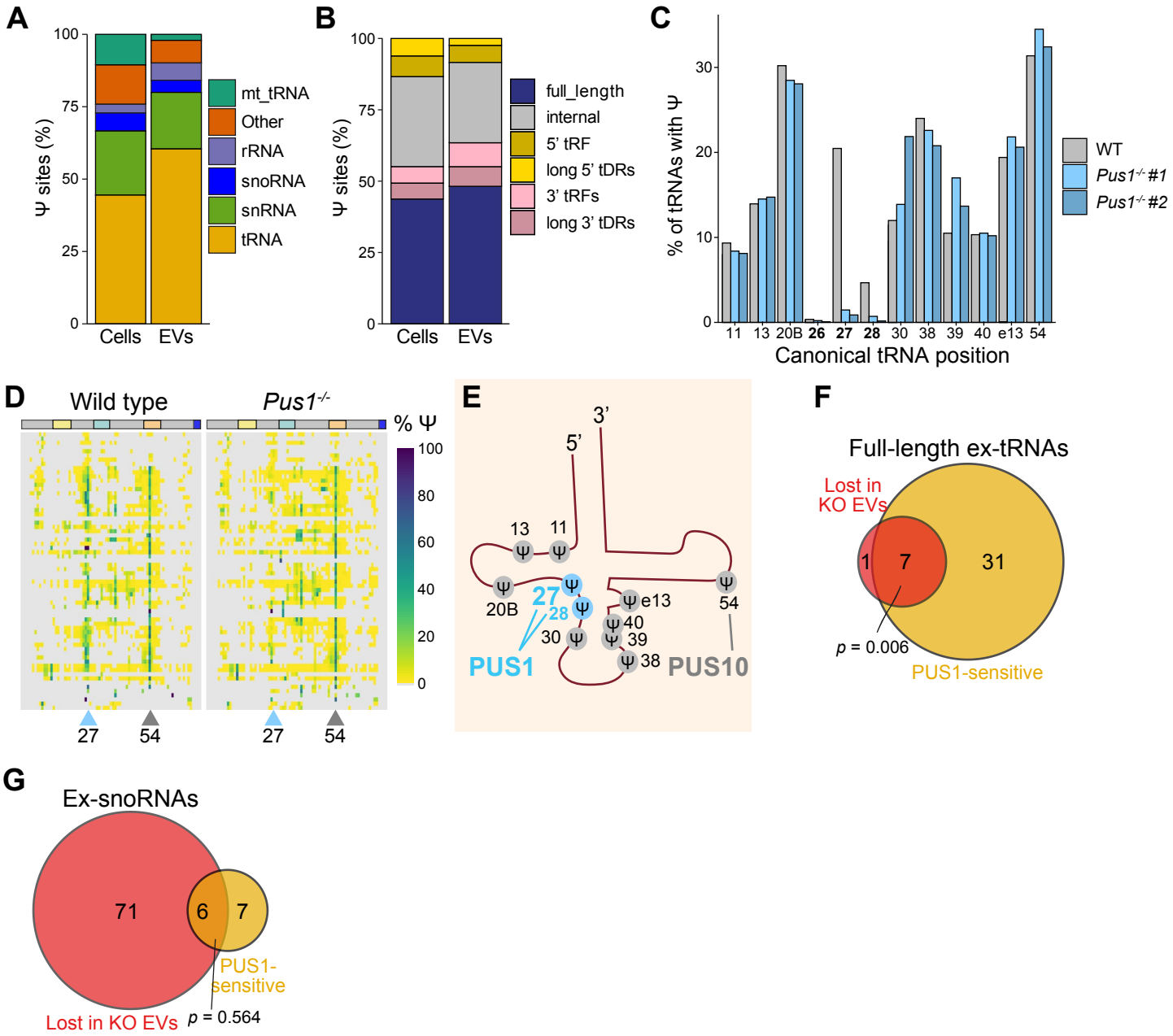


**Figure S5. Analyses on exRNAs from Pus1-/- CADs**

(A) Distribution of transcripts containing PUS1-sensitive Ψ sites in CADs and EVs among the indicated RNA classes. Data from 2 biological replicates.

(B) Distribution of reads containing PUS1-sensitive Ψ sites and mapping to tRNAs genes among the indicated types of tRNA-derived species in cells and EVs.

(C) % of Ψ modification detected at each canonical tRNA position in wild type or Pus1-/- CAD EVs. Data from the two different Pus1-/- clones are shown separately.

(D) % of Ψ at every canonical tRNA position (column) for every tRNA iso-acceptor containing a U at position 27 (rows) in EVs from wild type (left) or Pus1-/- (right) CADs.

(E) Scheme of canonical Ψ sites on tRNAs. In blue, Ψ sites dependent on PUS1.

(F) Overlap between significantly reduced full-length tRNAs in Pus1-/- (red) and PUS1 full-length tRNA targets (yellow) in EVs. P value is from a hypergeometric test.

(G) Same as (F) but for snoRNAs. For all panels data were from two biological replicates. In the case of Pus1-/- the two individual knockout clones were used as combined replicates.

For all panels data were from two biological replicates. In the case of Pus1-/- the two individual knockout clones were used as combined replicates (n = 2 per clone).

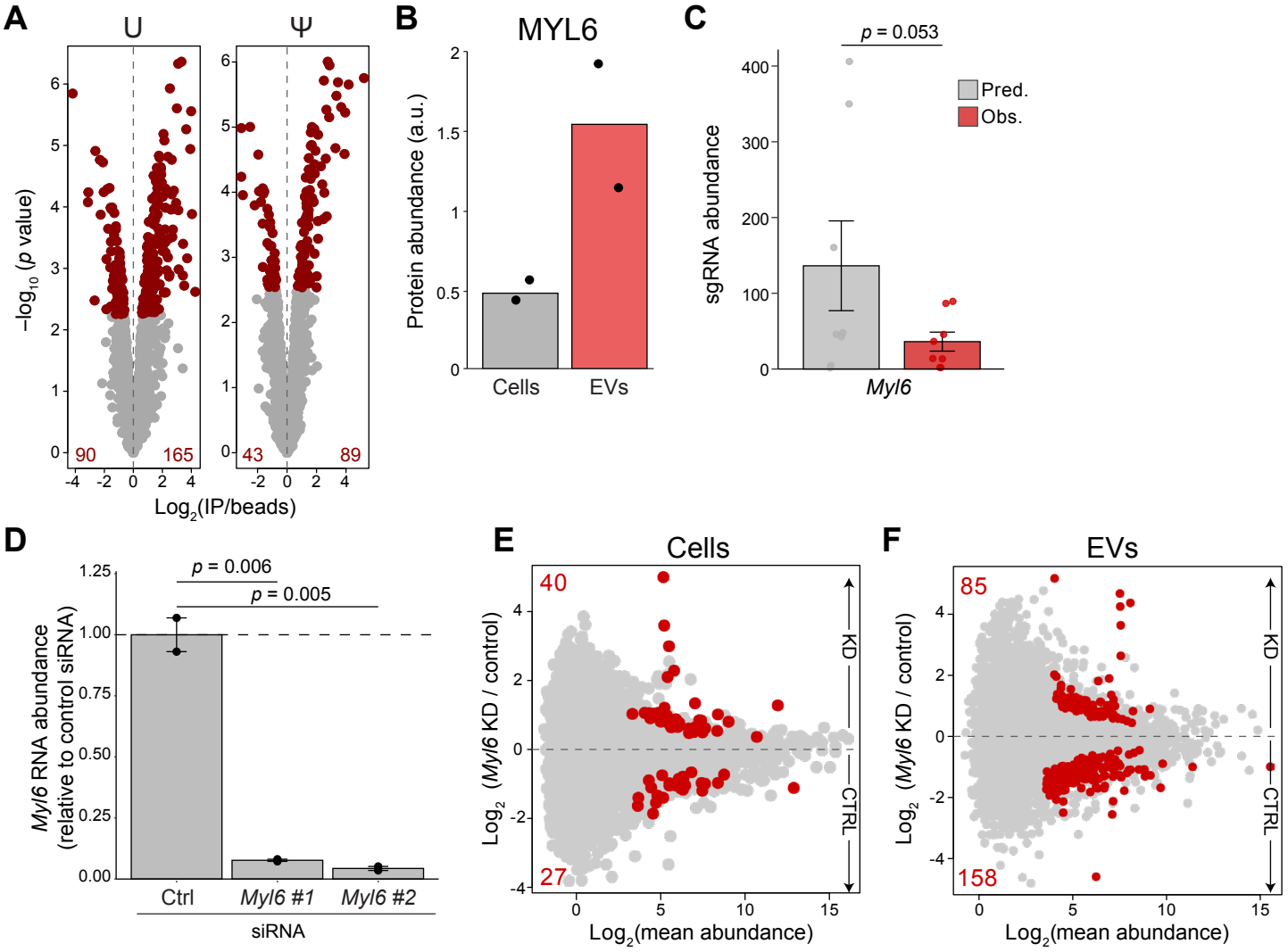


**Figure S6. Additional analyses for MYL6**

(A) IP/beads values for U- and Ψ-RNAs interactomes measured by mass spectrometry. In red, significantly different proteins (adjusted $p < 0.1$; $n = 2$).

(B) MYL6 protein abundance in CADs and EVs. Individual replicates are shown.

(C) Average predicted (gray) and observed (red) values ( SEM) for sgRNAs targeting Myl6. Circles represent individual sgRNAs. The p value is from MaGECK analysis.

(D) Myl6 mRNA abundance relative to control (Rpl32). Bars show average SEM. Individual replicates are shown. P values are from a Student's t test

(E) Differences in intracellular RNA abundance between control and Myl6 knockdown (KD) as measured by LIDAR. Red, transcripts showing significant difference (adjusted $p < 0.1$; $n \geq 2$).

(F) Same as (E) but for RNAs contained in EVs.